Electrostatic solitary waves and electrostatic waves at the magnetopause

D. B. Graham[1], Yu. V. Khotyaintsev[1], A. Vaivads[1], and M. André[1]

An edited version of this paper was published by AGU. Graham, D. B., Y. V. Khotyaintsev, A. Vaivads, and M. Andr (2016), Electrostatic solitary waves and electrostatic waves at the magnetopause, J. Geophys. Res. Space Physics, 121, 30693092, doi:10.1002/2015JA021527. To view the published open abstract, go to http://dx.doi.org and enter the DOI.

---

[1]Swedish Institute of Space Physics,

Uppsala, Sweden.

Abstract. Electrostatic solitary waves (ESWs) are characterized by localized bipolar electric fields parallel to the magnetic field, and are frequently observed in space plasmas. In this paper a study of ESWs and field-aligned electrostatic waves, which do not exhibit localized bipolar fields, near the magnetopause is presented using the Cluster spacecraft. The speeds, length scales, field strengths, and potentials are calculated and compared with the local plasma conditions. A large range of speeds is observed, suggesting different generation mechanisms. In contrast, a smaller range of length scales normalized to the Debye length λ_D is found. For ESWs the average length between the positive and negative peak fields is $9\,\lambda_D$, comparable to the average half wavelength of electrostatic waves. Statistically, the lengths and speeds of ESWs and electrostatic waves are shown to be similar. The length scales and potentials of the ESWs are consistent with predictions for stable electron holes. The maximum ESW potentials are shown to be constrained by the length scale and the magnetic field strength at the magnetopause and in the magnetosheath. The observed waves are consistent with those generated by the warm bistreaming instability, beam-plasma instability, and electron-ion instabilities, which account for the observed speeds and length scales. The large range of wave speeds suggests that the waves can couple different electron populations and electrons with ions, heating the plasma and contributing to anomalous resistivity.

1. Introduction

Electrostatic solitary waves (ESWs) are frequently observed in space plasmas. For example, ESWs have been reported at Earth's magnetopause [*Cattell et al.*, 2002; *Matsumoto et al.*, 2003], magnetotail [*Matsumoto et al.*, 1994; *Cattell et al.*, 2005; *Khotyaintsev et al.*, 2010b], auroral regions [*Ergun et al.*, 1998a, b; *Mozer et al.*, 2015], magnetosheath [*Pickett et al.*, 2005], near the foreshock [*Behlke et al.*, 2004; *Shin et al.*, 2008], and in the solar wind [*Mangeney et al.*, 1999; *Malaspina et al.*, 2013]. ESWs are also observed in laboratory experiments [*Fox et al.*, 2008; *Lefebvre et al.*, 2011]. At the magnetopause and magnetotail ESWs are often argued to be associated with magnetic reconnection [*Lapenta et al.*, 2011]. Magnetic reconnection provides the unstable electron distributions and/or strong currents required to generate ESWs [*Drake et al.*, 2003; *Divin et al.*, 2012].

ESWs are typically characterized by isolated bipolar electric fields, which are aligned with the background magnetic field $\mathbf{B}$ [*Matsumoto et al.*, 1994]. ESWs are consistent with Berstein-Greene-Kruskal (BGK) modes [*Bernstein et al.*, 1957], where a trapped electron or ion population supports a local potential maximum or minimum. ESWs have typically been found to be positive potential structures, i.e., electron holes [*Cattell et al.*, 2002; *Franz et al.*, 2005], with trapped electrons supporting the potential, although negative potential ion holes have also been observed, for instance in the auroral regions and near the foreshock [*Dombeck et al.*, 2001; *Behlke et al.*, 2004]. Simulations show that ESWs are stable in one dimension [*Omura et al.*, 1994; *Mottez et al.*, 1997], but in two or three dimensions ESWs require sufficiently large $\mathbf{B}$ to remain stable [*Miyake et al.*, 1998; *Muschietti et al.*, 2000; *Singh et al.*, 2001; *Lu et al.*, 2008]. When $\mathbf{B}$ is too weak a self-

focusing transverse instability develops and the ESWs are quickly dissipated [*Muschietti et al.*, 2000; *Wu et al.*, 2010]. Similarly, simulations show that large-amplitude ESWs can decay into other waves, such as ion-acoustic waves, lower-hybrid waves, and whistler waves [*Oppenheim et al.*, 2001; *Berthomier et al.*, 2002; *Dyrud and Oppenheim*, 2006].

The mechanisms responsible for the generation of ESWs have been studied extensively using simulations [*Omura et al.*, 1996]. Instabilities that can lead to the formation of ESWs include the bump-on-tail instability, beam-plasma instability, electron bistream instability, Buneman instability, lower-hybrid instability, and the modified two-stream instability [*Buneman*, 1959; *Omura et al.*, 1996; *Matsukiyo and Scholer*, 2006; *Che et al.*, 2009, 2010]. Recently, *Norgren et al.* [2015a] showed that dense subthermal electron beams interacting with the background ions can generate slow ESWs, with speeds comparable to the ion thermal speed. The ESW speeds have been shown to depend on the instability generating them. For instance, the Buneman instability is known to produce slow ESWs [*Drake et al.*, 2003; *Goldman et al.*, 2008; *Khotyaintsev et al.*, 2010b], well below the electron thermal speed v_e, whereas bump-on-tail and lower-hybrid instabilities can produce fast ESWs, with speeds comparable to or exceeding v_e [*Omura et al.*, 1996; *Che et al.*, 2010]. Therefore, observations of ESW speeds may provide clues to which instabilities are occurring.

Once ESWs are produced they can interact with background electrons. Fast ESWs produced by electron beams will tend to thermalize the beam and scatter background electrons with thermal energies comparable to the beam, effectively coupling different electron populations. Slow ESWs can couple electrons and ions, contributing to anomalous resistivity and reducing current densities [*Goldman et al.*, 2008; *Fujimoto et al.*, 2011].

Both spacecraft observations and simulations show that ESWs with distinct properties can be observed simultaneously, meaning that particle scattering can occur over a large range of particle energies [*Cattell et al.*, 2002; *Goldman et al.*, 2008; *Che et al.*, 2010; *Fujimoto*, 2014; *Graham et al.*, 2015].

ESWs are frequently observed near Earth's dayside magnetopause. They have been observed at the magnetopause boundary [*Cattell et al.*, 2002; *Matsumoto et al.*, 2003], associated with asymmetric reconnection [*Tang et al.*, 2013; *Graham et al.*, 2015], near the center of flux ropes [*Øieroset et al.*, 2014], and in the magnetosheath [*Pickett et al.*, 2005]. In the reconnection diffusion region parallel electron heating and bistreaming electrons are observed, which can generate ESWs via bistreaming instabilities [*Pritchett*, 2005; *Goldman et al.*, 2008; *Jara-Almonte et al.*, 2014]. In the separatrices electron beams develop, leading to the formation of ESWs by beam and/or current-driven instabilities [*Drake et al.*, 2003; *Cattell et al.*, 2005; *Divin et al.*, 2012; *Fujimoto*, 2014].

One of the challenges of investigating ESWs is determining their speeds and length scales. In general, this requires simultaneous spatially separated measurements of the electric field. The time delay between the field measurements can then be used to estimate the speeds and length scales. Spatially separated electric fields can be obtained from the same spacecraft using different probe combinations or different antennas. This method has been used successfully to calculate speeds of ESWs and ion solitary waves [*Franz et al.*, 1998; *Dombeck et al.*, 2001; *Franz et al.*, 2005; *Khotyaintsev et al.*, 2010b]. The main limitation of this method is that fast ESW speeds are difficult to calculate. In rare cases when two spacecraft are closely separated, the ESW speeds can be calculated from the time delays between two spacecraft [*Pickett et al.*, 2008; *Norgren et al.*, 2015b]. ESW

speeds have also been calculated from the relative strengths of the electric and magnetic field perturbations. The magnetic field perturbations are primarily associated with the Lorentz field of a moving charge [*Ergun et al.*, 1998a; *Andersson et al.*, 2009; *Tao et al.*, 2011].

Previous statistical analyses often considered the ESW time scales and amplitudes, which can be obtained from a single electric field measurement [*Pickett et al.*, 2004, 2005]. *Pickett et al.* [2004] showed that the ESW field strengths tended to increase as the magnetic field increases. The main limitation of these studies is that the ESW speeds, length scales, and potentials cannot be calculated. A number of surveys have investigated the lengths, speeds, and potentials of ESWs [*Kojima et al.*, 1999; *Cattell et al.*, 2003; *Franz et al.*, 2005; *Andersson et al.*, 2009; *Tao et al.*, 2011]. However, the generation mechanisms remain uncertain. In this paper we investigate the properties of ESWs and field-aligned electrostatic waves at the dayside magnetopause using the Cluster spacecraft [*Escoubet et al.*, 2001], and investigate the instabilities responsible for their generation.

The outline of this paper is as follows: In section 2 we state the data used and our analysis techniques. Section 3 shows an example of ESWs and electrostatic waves observed on 28 April 2006. In section 4 we present statistical analyses of ESWs and electrostatic waves at the magnetopause and in the magnetosheath. In section 5 we investigate the instabilities responsible for the observed ESWs and electrostatic waves. Section 6 is the discussion and section 7 is the conclusion.

2. Data and Analysis methods

2.1. Instruments and Data Selection

In this paper we use data from the Cluster spacecraft: magnetic field **B** data from Fluxgate Magnetometer (FGM) [*Balogh et al.*, 2001], electron data from Plasma Electron and Current Experiment (PEACE) [*Johnstone et al.*, 1997], ion data from Cluster Ion Spectrometry (CIS) [*Reme et al.*, 1997], and electric field **E** data from Electric Field and Wave experiment (EFW) [*Gustafsson et al.*, 1997; *Khotyaintsev et al.*, 2010a].

In general, the ESW time scales near the magnetopause are too small to be resolved from standard burst mode data ($\sim$ 450 samples/s on EFW), so we only investigate waves recorded during the internal burst mode intervals. During EFW's internal burst mode the probe voltages in the spacecraft spin plane are recorded at either 9000 or 4500 samples/s over a 10 second period. For the 4500 samples/s mode the magnetic field fluctuations are sampled by the search coil at the same frequency. The opposing probe potentials are measured simultaneously by the analog-to-digital converters, so there are no time delays between these probes. We search for ESWs and field-aligned electrostatic waves between 2002 and 2010 at times when Cluster cross the magnetopause from January to May. Furthermore, to reliably estimate the phase speeds and length scales of the waves one of the probe pairs must be closely aligned with **B** at the time of the wave observations. Therefore, we only analyze waves when the following conditions are satisfied: (1) The angle between one probe pair and the projection of **B** onto the spin plane is less than 25° and (2) the out-of-plane $|\mathbf{B}|$ is less than the in-plane $|\mathbf{B}|$, i.e., $B_z < \sqrt{B_x^2 + B_y^2}$ in spacecraft (ISR2) coordinates. For the spacecraft spin period ($\sim 4\,\mathrm{s}$), one probe pair can satisfy these conditions for $\lesssim 0.5\,\mathrm{s}$. In the following sections we consider a *wave event* to be the time interval over which the probe alignment satisfies the above conditions and ESWs or electrostatic waves are observed. Therefore, a single internal burst mode interval

can have multiple wave events as different probe combinations become aligned with **B**. On the magnetospheric side of the magnetopause near the subsolar point B_z is typically the largest component of **B**, so wave observations are likely under represented here.

To reliably estimate the speeds and length scales we only use data when all 4 probes are operational, which means most of the waves we investigate are obtained from Cluster 2 and Cluster 4 (C2 and C4, respectively). We use data from Cluster 3 in 2002 and no data from Cluster 1 are used.

2.2. Wave analyses

To estimate the speeds and length scales of the ESWs and electrostatic waves we calculate the frequency-wave number power spectrum for each wave event. The method we use to calculate the power spectrum follows closely the method in *Dudok de Wit et al.* [1995]. We then fit the linear dispersion relation $\omega = vk$ to the spectrum over the frequency range where the power is most intense. The spectrum can be calculated when spatially separated measurements of **E** are available simultaneously. Here, we use the different probe combinations to obtain two spatially separated measurements of **E**. On Cluster the probes are numbered p1–p4, with orthogonal fields computed from p1 and p2, and p3 and p4. When two probes are closely aligned with **B** we compute the fields from the potential difference between these two probes and the spacecraft potential $V_{\rm SC}$, where $V_{\rm SC}$ is the average potential of the two remaining probes. This provides two measurements of the parallel electric field $\mathbf{E}_{\|}$ separated by approximately 44 m along **B** [*Khotyaintsev et al.*, 2010b]. The procedure we use is summarized as follows:

(1) We perform the wavelet transforms W_1 and W_2 of the two fields $\mathbf{E}_1$ and $\mathbf{E}_2$, respectively, calculated from the two probes aligned with **B** and $V_{\rm SC}$. We use the standard

Morlet wavelet function as the "mother" wavelet, to provide a good compromise between frequency and time resolution.

(2) We calculate the phase difference $\Delta\psi$ between the signals using the cross-spectrum between the fields:

$$C(t,f) = \langle W_1(f,t)W_2^*(f,t)\rangle, \tag{1}$$

where the angled brackets correspond to time averaging. The phase difference $\Delta\psi$ is then determined by the argument of $C(f,t)$, given by

$$\Delta\psi = \text{atan2}\left(\text{Im}[C(f,t)], \text{Re}[C(f,t)]\right). \tag{2}$$

The parallel wave number is $k_\parallel = \Delta\psi/(d\cos\theta)$, where θ is the angle between the probes and $\mathbf{B}$, and $d = 44\,\text{m}$ is the separation between the $\mathbf{E}_1$ and $\mathbf{E}_2$ measurements. We typically average over 128 points in time for each frequency, to reliably estimate $\Delta\psi$. This is typically much smaller than the total time interval of $\mathbf{E}_1$ and $\mathbf{E}_2$, so changes in the angle between the probes and $\mathbf{B}$ are taken into account when calculating v. Moreover, changes in the wave speed with time are resolved.

(3) We calculate the average power of $\mathbf{E}_1$ and $\mathbf{E}_2$

$$P(f,t) = \langle W_1W_1^* + W_2W_2^*\rangle/2. \tag{3}$$

We then bin $P(f,t)$ for each time interval according to f and $k_\parallel$ to obtain the frequency-wave number power spectrum $P(f,k)$.

(4) To calculate the speed of the waves we fit the linear dispersion relation

$$f = \frac{vk_\parallel}{2\pi}, \tag{4}$$

to the power spectrum over the frequency range where the observed powers are maximal. In general, the power spectra we obtain are approximately linear, so equation (4) provides

a good model to the data. Note that v in equation (4) is both the phase speed and group speed of the wave. The length scales can then be calculated from v and observed time scales.

For stable ESWs propagating across the spacecraft a linear dispersion relation given by equation (4) is expected. This can be understood as follows: ESWs are localized structures, which are stable over the time taken to cross the spacecraft [*Pickett et al.*, 2008; *Norgren et al.*, 2015b]. Therefore, the two electric fields constructed from the probe potentials should be approximately the same, except for a time delay Δt related to the ESW speed by $v = d\cos\theta/\Delta t$. When an ESW is studied in frequency space, using either Fourier or wavelet methods, the ESW is composed of a range of frequencies. For each frequency the time delay Δt between the fields is the same so the corresponding phase difference at a specific frequency f is given by $\Delta\psi = 2\pi f\Delta t$. It follows that $k_{\parallel} = 2\pi f\Delta t/(d\cos\theta) = 2\pi f/v$ from the above equations, from which we obtain equation (4). Therefore, for solitary structures we expect f to increase linearly with $k_{\parallel}$. Moreover, this method is equivalent to calculating v from the delays in the time series, but has the advantage of eliminating DC offsets and enables fast ESW speeds to be estimated. We tested this method using model data of a single ESW and background noise using the same cadence as EFW's internal burst mode. We are able to resolve ESW speeds up to $\sim 10000\,\mathrm{km\,s^{-1}}$ when the ESW amplitude is well above the noise level. As the amplitude of ESWs decreases compared with the background noise, the speed becomes more uncertain. Therefore, the above method is best suited to larger amplitude ESWs.

As an example we apply the above method to an isolated ESW observed by C2 on 3 March 2004. Figure 1a shows the electric fields $\mathbf{E}_{\mathrm{SC-p3}}$ and $\mathbf{E}_{\mathrm{p4-SC}}$ obtained from the

potential differences between probes 3 and 4 and the spacecraft potential. At this time the angle between **B** and probes 3 and 4 is 19° and **B** is directed from p3 to p4. Figure 1a shows that the ESW's electric field is observed by p4 before p3, meaning that the ESW propagates antiparallel to **B**, and the field diverges. Figure 1b shows $\mathbf{E}_{\mathrm{SC-p3}}$, and $\mathbf{E}_{\mathrm{p4-SC}}$ time shifted by 0.34 ms so the fields overlap. Based on this time delay we calculate the ESW speed to be $v = d\cos\theta/\Delta t = -122\,\mathrm{km\,s^{-1}}$, where Δt is the time shift between the fields. The minus sign indicates propagation antiparallel to **B**. Figure 1c shows the frequency-wave number power spectrum $P(f,k)/P_{\mathrm{max}}$ normalized to the maximum power for the ESW obtained from $\mathbf{E}_{\mathrm{SC-p3}}$ and $\mathbf{E}_{\mathrm{p4-SC}}$, using the above method. The frequencies of peak power increase approximately linearly with $k_{\|}$. The fit of equation (4) to the data, shown in Figure 1c, is $v = -126\,\mathrm{km\,s^{-1}}$. Therefore, the speed estimates from the time difference between fields and the dispersion relation are in excellent agreement, as expected from the above discussion. When multiple ESWs are observed the resulting power spectrum shows a single dispersion relation for ESWs with comparable speeds, but distinct dispersion relations are observed when the ESWs have distinct speeds [*Graham et al.*, 2015]. Here and in the following sections we use an automated fitting routine to calculate v. We find the least-squares fit to the points with $P(f,k) > 0.1P_{\mathrm{max}}$. The weightings used for each (f,k) point are $1+\log_{10}(P(f,k)/P_{\mathrm{max}})$. The accuracy of the fits are confirmed by visual inspection and where possible by estimating v from the observed time delays.

3. Example: Magnetopause crossing on 28 April 2006

As an example, we investigate in detail ESWs and electrostatic waves observed by C4 on 28 April 2006 after a crossing of Earth's magnetopause. Figures 2a–2d present an

overview of the magnetopause crossing, showing $\mathbf{B}$, the bulk ion velocity $\mathbf{V}$ (obtained from the ion moments), the electron number density n_e, and the electron differential energy flux. C4 crossed the magnetopause from the magnetosphere into a plasma dominated by magnetosheath electrons at 03:22:00 UT, as indicated by the change in direction of $\mathbf{B}$, increase in n_e, and decrease in the electron temperature T_e. C4 was located at $(6.1, -4.7, 3.7)R_E$ in Geocentric Solar Magnetospheric (GSM) coordinates at the time of the magnetopause crossing. Throughout most of the interval after the magnetopause crossing magnetospheric electrons remain, indicating mixing of magnetospheric and magnetosheath electrons. Only after 03:45:00 UT are there time intervals with negligible high-energy electrons, corresponding to the unperturbed magnetosheath, where no magnetospheric electrons are observed. Figure 2b shows that the ion speed V reaches a maximum of $\sim 200\,\mathrm{km\,s^{-1}}$ northward, close to the magnetopause boundary. In the unperturbed magnetosheath, outside the region where magnetic reconnection is occurring and no magnetospheric electrons are observed, $V \sim 80\,\mathrm{km\,s^{-1}}$. Throughout this time interval the solar wind B_z is southward, consistent with magnetic reconnection occurring at the dayside magnetopause, with C4 encountering the northward outflow. This explains the observed mixing of magnetospheric and magnetosheath electrons.

The blue shaded interval in Figures 2a–2c shows the time when EFW was operating in internal burst mode. Just before this there is an increase in electron flux at magnetospheric energies. The internal burst mode was triggered just before a current sheet, where B_y reverses direction. During this time we observe both ESWs and field-aligned electrostatic waves. Figures 2e and 2f show the time series of $\mathbf{E}_\parallel$ and $\mathbf{E}_\perp$ and the spectrogram of $\mathbf{E}_\parallel$ when the waves were observed. We define $\mathbf{E}_\parallel$ to be the component of $\mathbf{E}$ parallel to the

projection of $\mathbf{B}$ onto the spin plane and $\mathbf{E}_\perp$ to be the remaining component of $\mathbf{E}$ in the spin plane, which is perpendicular to $\mathbf{E}_\parallel$ and $\mathbf{B}$. At this time the electron temperature T_e is $\approx 80\,\mathrm{eV}$ and the electron number density n_e is $\approx 9\,\mathrm{cm}^{-3}$. The time series shows that the waves are approximately parallel to $\mathbf{B}$; for the high-frequency oscillations $\mathbf{E}_\parallel \gg \mathbf{E}_\perp$, indicating that the ESWs are oblate (pancake shaped) with minor axis along $\mathbf{B}$. This is consistent with ESWs in a weakly magnetized plasmsa [*Franz et al.*, 2000]. Figure 2f shows that two different wave frequencies are observed. Before 03:41:35.5 UT (left side) the waves have maximum power frequencies at $\sim 1\,\mathrm{kHz}$, above the ion plasma frequency f_{pi} and below electron cyclotron frequency f_{ce}. After 03:41:35.5 UT (right side) the waves have maximum power at $\sim 500\,\mathrm{Hz}$, just below f_{pi}.

The waves on the left and right side of Figure 2e have different waveforms, as shown in Figures 2g and 2h. On the left, the waves consist of distinct bipolar fields, as expected for ESWs. Each ESW has $+/-$ polarity, indicating that they propagate in the same direction. On the right, the electrostatic waves are much more periodic, although they differ from sinusoidal waves. Some of the oscillations away from the center of Figure 2h appear to have fields similar to ESWs, and where the waves are most intense, evidence for plateaux between the wave periods start to develop. This may correspond to ESWs beginning to develop for more periodic sinusoidal waves.

At the time these waves are observed probes 3 and 4 are closely aligned with $\mathbf{B}$, so we can construct the fields $\mathbf{E}_{\mathrm{p3-SC}}$ and $\mathbf{E}_{\mathrm{SC-p4}}$, which are approximately field aligned, with $\mathbf{B}$ pointing from p4 to p3. Figures 2i and 2j show $\mathbf{E}_{\mathrm{p3-SC}}$ and $\mathbf{E}_{\mathrm{SC-p4}}$ for the ESWs and electrostatic waves, respectively. In both cases $\mathbf{E}_{\mathrm{SC-p4}}$ is observed before $\mathbf{E}_{\mathrm{p3-SC}}$, corresponding to wave propagation parallel to $\mathbf{B}$. For the ESWs this means that the

electric fields are diverging, so the ESWs are positive potential structures, i.e., electron holes. In Figures 2i and 2j the time domains are equal, so the larger delay between $\mathbf{E}_{\mathrm{SC-p4}}$ and $\mathbf{E}_{\mathrm{p3-SC}}$ in Figure 2j means that the electrostatic waves propagate slower than the ESWs.

For the time series in Figure 2d probes 3 and 4 satisfy the criteria in section 2.1, so we construct the frequency-wave number spectrum from $\mathbf{E}_{\mathrm{p3-SC}}$ and $\mathbf{E}_{\mathrm{SC-p4}}$. Figure 3 shows the resulting power spectrum normalized to the maximum power $P(f,k)/P_{\max}$, using the method in section 2.2. We observe two distinct dispersion relations. Both dispersion relations are approximately linear, and using fits to the data we obtain speeds of $v \approx 220\,\mathrm{km\,s^{-1}}$ and $v \approx 680\,\mathrm{km\,s^{-1}}$. Calculations of the spectrum over shorter times show that the faster mode is the ESWs and the slower mode is the electrostatic waves, as expected from the time delays in Figures 2i and 2j. The fact that the ESW power spectrum is very narrow indicates that all the ESWs have comparable speeds. The range of parallel wave numbers $k_{\parallel}$ where the power is maximal is similar for the ESWs and electrostatic waves, suggesting they have comparable length scales.

For the ESWs the average peak-to-peak time is $\tau_{pp} = 0.29\,\mathrm{ms}$. Note that the frequencies associated with the ESWs in Figure 2f is determined by τ_{pp}, which are determined by the ESW length scales and the relative speed of the ESWs to the spacecraft. The average peak-to-peak length l_{pp}, which is defined as the distance between the positive and negative peaks of the ESWs, is then $l_{pp} = v\tau_{pp} = 200\,\mathrm{m}$ or $9.1\,\lambda_D$, where $\lambda_D = 22\,\mathrm{m}$ is the Debye length. This length scale is comparable to previous ESW observations [*Khotyaintsev et al.*, 2010b; *Graham et al.*, 2015]. For the electrostatic waves in Figure 2g the average wave period is $T = 2.8\,\mathrm{ms}$, so the corresponding wavelength is $\lambda = 620\,\mathrm{m} = 28\,\lambda_D$. For the

ESWs l_{pp} corresponds to half a wavelength, so the electrostatic waves have length scales approximately 1.5 times longer than the ESWs. In the following sections we use this method to estimate v and l_{pp} of ESWs and electrostatic waves for each wave event. We note that the calculated v are the wave speeds in the spacecraft frame. At the time the waves are observed the projection of $\mathbf{V}$ along $\mathbf{B}$ is $\approx 100\,\mathrm{km\,s^{-1}}$. So in the ion frame the ESW and electrostatic wave speeds are $\approx 580\,\mathrm{km\,s^{-1}}$ and $\approx 120\,\mathrm{km\,s^{-1}}$, respectively. Therefore, the ESWs propagate approximately five times faster than the electrostatic waves.

These observations raise the question of whether the ESWs and electrostatic waves in Figures 2 and 3 are produced by the same or different instabilities. It is natural to assume that the ESWs correspond to a late stage of evolution, when isolated bipolar fields have developed and the spacing between each ESW becomes irregular, whereas the electrostatic waves correspond to an earlier stage of evolution when ESWs are starting to develop from more periodic electrostatic waves. This would mean the ESWs and electrostatic waves develop at slightly different times. Because the waves are observed with distinct speeds and no evidence of waves with intermediate speeds is observed in Figure 3, the waves are unlikely to be accelerating or decelerating significantly. This suggests that the waves are produced by different instabilities [*Graham et al.*, 2015].

We now compare the observed speeds with theoretical predictions. When the waves are observed we calculate the electron thermal speed to be $v_e = \sqrt{2q_eT_e[\mathrm{eV}]/m_e} = 5300\,\mathrm{km\,s^{-1}}$, where q_e and m_e are the electron charge and mass, respectively. The observed wave speeds are well below v_e, meaning that thermal or superthermal electron beams cannot produce the observed waves through Landau resonance. At the time the

waves are observed the ion thermal speed is $v_i \approx 300\,\mathrm{km\,s^{-1}}$. This might indicate that the ESWs are generated by electron-ion instabilities [*Norgren et al.*, 2015a]. The slower waves have speeds below v_i, so might be generated by the warm-bistream instability, as discussed in section 5.

4. Statistical Analyses

In this section we investigate the wave properties and compare them with the local plasma conditions. For each wave event, where the conditions in section 2.1 are satisfied, we calculate the phase speeds and length scales from the frequency-wave number power spectra. We divide the waveforms into two groups: ESWs and field-aligned electrostatic waves. We classify the electric fields as ESWs when isolated bipolar $\mathbf{E}_{\parallel}$ are observed. We classify the electric fields as electrostatic waves when the fluctuations are aligned with $\mathbf{B}$, and isolated bipolar $\mathbf{E}_{\parallel}$ are not observed. Although $\mathbf{E}$ is only measured in two dimensions, the lack of strong fluctuations in the measured $\mathbf{E}_{\perp}$ direction suggests that the waves are generally field-aligned. When search coil data are available, no magnetic field fluctuations are observed at the same frequencies as the ESWs or the electrostatic waves, indicating that these waves are electrostatic. Therefore, since the waves are electrostatic and $\mathbf{E}$ is expected to be closely aligned with $\mathbf{B}$, we expect the wave vector to be closely aligned with $\mathbf{B}$. For electrostatic waves, when the waveform is quasiperiodic we calculate λ from the wave's speed and period; when the waveform is not quasiperiodic and the period cannot be obtained we calculate $\lambda = 2\pi/k_{\parallel}$, where $k_{\parallel}$ is the wave number where the power is maximal.

In Figure 4a we plot the local T_e versus n_e obtained from the electron moments for each wave event. Our survey includes regions of predominantly magnetospheric electrons,

regions of magnetospheric and magnetosheath electron mixing, and regions of magnetosheath electrons. The electron temperature tends to decrease as the proportion of magnetosheath electrons increases. As a result, T_e tends to decrease as n_e increases. There is a much larger proportion of electrostatic waves for low T_e and high n_e, corresponding to a plasma dominated by magnetosheath electrons. For $n_e > 20\,\mathrm{cm}^{-3}$ only electrostatic waves are observed in our survey and very few electrostatic waves are observed for high T_e and low n_e.

4.1. Wave speeds and length scales

In this subsection we investigate the speeds and length scales of ESWs and electrostatic waves and compare them with the local plasma conditions. In Figure 4b we plot the wave speed v versus the peak-to-peak length l_{pp} of ESWs and half wavelength $\lambda/2$ of electrostatic waves for each wave event. The solid black line corresponds to $\tau_{pp} = 0.11\,\mathrm{ms}$. The region below the line corresponds to observable ESWs and electrostatic waves. Statistically, v increases with l_{pp}. In particular, the minimum observed v tends to increase with l_{pp} and $\lambda/2$. One of the main limitations of this survey is the time resolution of EFW's internal burst mode, which has a maximum sampling rate of 9000 samples/s when potentials from all four probes are available (most ESWs and electrostatic waves were observed in this mode). Assuming the minimum τ_{pp} observable corresponds to the time between adjacent field measurements, then $\tau_{pp} = 0.11\,\mathrm{ms}$. Therefore, as l_{pp} increases faster waves can be resolved, partly explaining the statistical trend. The sampling rate restricts our observations to waves with $v < v_e$.

Figures 5a–5c show v for ESWs and electrostatic waves versus T_e, n_e, and λ_D, respectively, for each wave event. Here v is calculated in the spacecraft frame. The range of v

spans over two orders of magnitude from $\sim 20\text{km}\,\text{s}^{-1}$ to $\sim 5000\text{km}\,\text{s}^{-1}$, larger than the range of speeds reported by *Cattell et al.* [2003]. Statistically, the speeds increase with T_e and λ_D, and decrease as n_e increases. The decrease in v as n_e increases may be due to associated statistical decrease in T_e (Figure 4a). However, the large range of v for similar plasma conditions suggests that multiple instabilities are generating the observed waves [*Graham et al.*, 2015]. Many of the observed waves have speeds comparable to or smaller than the nominal v_i assuming $T_i/T_e = 5$, indicating slow propagation speeds. Overall, the electrostatic waves tend to have smaller speeds than the ESWs, although there is significant overlap in the speeds for low T_e and high n_e.

In Figure 5d we plot l_{pp} for ESWs and $\lambda/2$ for electrostatic waves versus λ_D. Figure 5d shows that l_{pp} and $\lambda/2$ increase linearly with λ_D. As a result, there is no observed statistical trend in l_{pp}/λ_D or $\lambda/2\lambda_D$ when plotted versus n_e or T_e, as seen in Figures 5e and 5f. This indicates that l_{pp} and $\lambda/2$ are primarily determined by the local λ_D. For the ESWs we calculate a mean l_{pp} of $8.6 \pm 3.8\,\lambda_D$ (overplotted in Figure 5d). Note that the mean parallel characteristic length scale is then $l_\parallel = l_{pp}/2 = 4.3\,\lambda_D$. For the electrostatic waves the mean $\lambda/2$ is $9.6 \pm 5.5\,\lambda_D$. Therefore, both ESWs and electrostatic waves have on average comparable length scales. We find no correlation between l_{pp}/λ_D or $\lambda/2\lambda_D$ with v or v/v_e, suggesting that the length scales normalized to λ_D do not depend on v for the observed range of phase speeds. The estimated length scales are in good agreement with previous observations (e.g., *Cattell et al.* [2003] and *Franz et al.* [2005]), although they tend to be smaller than those reported by *Andersson et al.* [2009] and *Tao et al.* [2011] in the magnetotail. The speeds are statistically smaller than those found in *Franz et al.* [2005]; however, this may be because we cannot resolve waves with $v \gtrsim v_e$.

In Figure 5 many of the ESWs and electrostatic waves have speeds comparable to or smaller than typical ion flow speeds in the magnetosheath. Therefore, it is necessary to calculate the wave speeds in the ion frame using $v' = v - \mathbf{V}\cdot\mathbf{B}/|\mathbf{B}|$, where the final term is the ion flow speed parallel to $\mathbf{B}$. For electron-ion instabilities, for instance, the Buneman instability, the predicted speeds correspond to those observed in the ion frame, so the speeds can only be compared with predictions in the ion frame. For C3 and C4 we use the ion velocity moments from CIS-HIA and CIS-CODIF, respectively. The ion moments are computed once per spacecraft spin ($\sim 4\,\mathrm{s}$), so there is some uncertainly in the flow speed at the time the waves are observed because of the low sampling rate. This uncertainty is largest for small v'; for the fast waves this uncertainty is negligible. However, the variation in ion speeds between adjacent points in the time series is too small to change the statistical results. Ion data are unavailable on C2, so we use ion data from the closest spacecraft when the separation is $\lesssim 200\,\mathrm{km}$ and plasma conditions are similar between the spacecraft. Figure 6 shows the phase speeds v' in the ion frame. Statistically, the results are similar to Figures 5a and 5b. For waves with high phase speeds, in particular, for the low-density high-temperature plasmas, the ion flow is negligible compared with the wave's phase speed. Many of the waves have speeds below v_i in the ion plasma frame. Figure 6 also shows ESWs and electrostatic waves with speeds as low as $10\,\mathrm{km\,s^{-1}}$, which means that the waves are almost stationary in the ion frame. These waves were observed for lower T_e when the magnetosheath electrons dominate. To our knowledge this is the first time such slow ESWs and electrostatic waves have been recorded. The slowest ESWs and electrostatic waves have speeds well below the speeds the typical ion thermal speed $v_i \sim 200\,\mathrm{km\,s^{-1}}$ in the magnetosheath, suggesting that the speeds are too

small to be produced by electron-ion streaming instabilities. We propose that these waves may be generated by the warm bistream instability [*Omura et al.*, 1996; *Mottez et al.*, 1997], where the counter-propagating electrons have very similar properties. We discuss the warm bistream instability in detail in section 5.1.

We now investigate how the waves depend on the local magnetic field strength B and n_e. For all the wave events we observe at the magnetopause and in the magnetosheath the plasma is weakly magnetized, i.e., $\omega_{pe}/\Omega_{ce} > 1$, where ω_{pe} is the angular electron plasma frequency and Ω_{ce} is the angular electron cyclotron frequency. Figure 7a shows a scatterplot of B and n_e for each wave event. We observe a significantly higher proportion of ESWs compared with electrostatic waves at lower n_e and higher B. Whereas most electrostatic waves are observed for higher n_e and lower B. That is, as the plasma becomes more weakly magnetized we are less likely to observe ESWs, and more likely to observe field-aligned electrostatic waves.

In Figure 7b we plot the maximum peak-to-peak electric field strength E_{pp} of ESWs and electrostatic waves for each wave event versus ω_{pe}/Ω_{ce}. Figure 7b shows that for ESWs E_{pp} tends to decrease as ω_{pe}/Ω_{ce} increases, indicating that larger amplitude ESWs are observed in more strongly magnetized plasmas. Qualitatively, this result is consistent with *Pickett et al.* [2004]. No ESWs are observed in our survey for plasmas with $\omega_{pi}/\Omega_{ce} > 1$, where ω_{pi} is the angular ion plasma frequency. This suggests that when the plasma is too weakly magnetized ESWs are no longer stable. For electrostatic waves there does not appear to be any dependence of E_{pp} on ω_{pe}/Ω_{ce}, although most electrostatic waves are found in a narrow domain. For $\omega_{pi}/\Omega_{ce} \ll 1$ very few electrostatic waves are observed. We consider the stability of ESWs in detail in the following subsection.

In summary, the phase speeds tend to increase with increasing T_e and decreasing n_e, although a range of speeds are observed for a given T_e, n_e, or λ_D. This suggests that multiple instabilities are occurring near the magnetopause. Statistically, l_{pp} and $\lambda/2$ increase linearly with λ_D, meaning l_{pp}/λ_D and $\lambda/2\lambda_D$ do not appear to depend on the plasma conditions. The similarity between the properties of the ESWs and electrostatic waves suggests that the same instabilities may be responsible for both waves. ESWs may develop from the nonlinear evolution of electrostatic waves as electrons become trapped in the wave potentials. When the plasma is too weakly magnetized we no longer observe ESWs in our survey.

4.2. Wave amplitudes and potentials

In this subsection we compare the maximum field strengths and potentials of ESWs and electrostatic waves with the local plasma conditions. For ESWs we assume that the potential along **B** is

$$\phi = \phi_{\mathrm{ESW}} \exp\left(\frac{-x^2}{2l_{\parallel}^2}\right), \tag{5}$$

where ϕ_{ESW} is the ESW maximum potential and $l_{\parallel} = l_{pp}/2$ is the characteristic length. The maximum observed potential can be calculated from E_{pp} and l_{pp}, and is given by

$$\phi_{\mathrm{ESW}} = \frac{E_{pp} l_{pp} \mathrm{e}^{1/2}}{4}. \tag{6}$$

To calculate the observed potential of the electrostatic waves we assume a sinusoidal wave: $E(x,t) = E_0 \sin(\omega t - kx)$. The maximum potential of the electrostatic waves is then

$$\phi_{\mathrm{ES}} = \frac{E_{pp}\lambda}{4\pi}, \tag{7}$$

where $\lambda = 2\pi/k$ is the wavelength. For each wave event we calculate the potentials using the largest E_{pp}, corresponding to the largest observed potential.

We plot the maximum E_{pp} versus T_e and n_e for each wave event in Figures 8a and 8b. We find that the range of E_{pp} is $1\,\mathrm{mV\,m^{-1}} \lesssim E_{pp} \lesssim 50\,\mathrm{mV\,m^{-1}}$ for both ESWs and electrostatic waves. Statistically, there is little difference in E_{pp} for ESWs and electrostatic waves, although for ESWs there appears to be a slight statistical increase in E_{pp} as T_e increases and n_e decreases. Similarly, there is a slight increase in E_{pp} with λ_D (not shown), but this trend is small. For electrostatic waves a dependence on T_e, n_e, or λ_D is difficult to determine because electrostatic waves are primarily observed for low T_e and high n_e.

The maximum observed potentials $\phi_{\mathrm{ESW,ES}}$ for ESWs and electrostatic waves are shown in Figures 8c–8e versus T_e, n_e, and λ_D, respectively. Electrostatic waves tend to have smaller potentials than ESWs, although electrostatic waves are primarily observed for large n_e. Statistically, $\phi_{\mathrm{ESW,ES}}$ increases as T_e increases and $\phi_{\mathrm{ESW,ES}}$ decreases as n_e increases. The increase in the ESW potentials is approximately proportional to λ_D, as shown in Figure 8e. This occurs because E_{pp} depends weakly on T_e and n_e (and hence λ_D), and l_{pp} and $\lambda/2$ increase proportionally with λ_D, so ϕ increases according to equations (6) and (7).

We normalize the maximum potentials to the background T_e, $q_e\phi_{\mathrm{ESW,ES}}/k_BT_e$. Figure 8f shows $q_e\phi_{\mathrm{ESW,ES}}/k_BT_e$ versus λ_D. There is little statistical change in $q_e\phi_{\mathrm{ESW,ES}}/k_BT_e$ with λ_D. Similarly, $q_e\phi_{\mathrm{ESW,ES}}/k_BT_e$ does not change with T_e or n_e (not shown). In most cases we find that $10^{-3} \lesssim q_e\phi_{\mathrm{ESW,ES}}/k_BT_e \lesssim 10^{-2}$, meaning individual ESWs interact weakly with the background electron population. These values of $q_e\phi_{\mathrm{ESW,ES}}/k_BT_e$ are in agreement with the ESWs reported by *Cattell et al.* [2003] and *Franz et al.* [2005] in the

cusp region. In some cases, such as Figure 2, a large number of ESWs are observed over a very short time interval, meaning an electron can interact with multiple ESWs, thus making electron scattering and heating significant. The range of electron speeds trapped in the ESW potentials is $\sim v \pm v_T$, where $v_T = \sqrt{2q_e\phi_{\rm ESW}/m_e}$ is the electron trapping speed. Based on Figures 8e and 8f, $v_T/v_e = \sqrt{q_e\phi/k_BT_e} \sim 0.1$. This indicates that a small fraction of the total electron population is trapped in the ESW potentials. The small v_T means that when ESW speeds differ significantly the faster ESWs can propagate through slower ESWs without coalescence because the speeds of trapped electrons do not overlap [*Umeda et al.*, 2002]. This explains how distinct ESW speeds can occur at the magnetopause [*Cattell et al.*, 2002; *Graham et al.*, 2015]. In general, the observed potentials are sufficiently small that they do not interact strongly with ions [*Drake et al.*, 2003].

We now investigate whether the observed potentials and length scales are consistent with predictions for stable electron phase-space holes. In Figure 9a we plot $q_e\phi_{\rm ESW,ES}/k_BT_e$ versus l_{pp}/λ_D and $\lambda/2\lambda_D$, for ESWs and electrostatic waves, respectively. Overplotted is the line corresponding to the maximum allowable $q_e\phi/k_BT_e$ for a given l_{pp}/λ_D using equation (11) of *Chen et al.* [2005]. This condition was derived from the time-stationary Vlasov-Poisson equations, based on the requirement that the ESW potential is supported by a trapped particle distribution, which cannot take negative values. We assume $T_e/T_i = 0.5$ and the ratio of the perpendicular to parallel length scale $l_r/l_\parallel = 4$. In most cases the changes in $\mathbf{E}_\perp$ are very small compared with $\mathbf{E}_\parallel$, indicating that l_r is significantly larger than $l_\parallel$ [*Franz et al.*, 2000]. In general, the typical values of T_e/T_i are smaller than 0.5 at the magnetopause and in the magnetosheath, and $l_r/l_\parallel$ will often be greater than 4 based

on the typical relative strengths of $\mathbf{E}_{\parallel}$ and $\mathbf{E}_{\perp}$. Therefore, the chosen values of T_e/T_i and $l_r/l_{\parallel}$ place the strictest constraints on the region of allowable values of $q_e\phi/k_BT_e$. Figure 9a shows that all observed ESWs and electrostatic waves occupy the region of allowable ESWs. Moreover, the values $q_e\phi_{\mathrm{ESW,ES}}/k_BT_e$ are the maximums for each wave event, so the individual ESWs with lower amplitudes associated with each wave event will be further below the threshold condition. Since all the electrostatic waves also occur in the stable region, they should be able to trap electrons, enabling the formation of ESWs. Finally, we note that ESW speed can modify the region of stable ESWs. In particular, as the ESW speed increases the minimum allowed length scale will increase [*Chen et al.*, 2005]. However, this constraint only becomes significant for $v > v_e$, so for the ESWs we observe with $v < v_e$, this constraint has negligible effect on the allowed length scales.

The fact that almost all observed $q_e\phi_{\mathrm{ESW,ES}}/k_BT_e$ are well below the predicted maximum value suggests that there are additional constraints on the values of $q_e\phi_{\mathrm{ESW,ES}}/k_BT_e$. In particular, the ESWs are observed in weakly magnetized plasmas, which means that the electron motion perpendicular to $\mathbf{B}$ could be important. For the ESWs observed at the magnetopause and in the magnetosheath the electron Larmor radius ρ_e is typically larger than the observed l_{pp} and could be comparable to l_r. Therefore, the trapped electrons supporting the ESW potentials could escape in the directions perpendicular to $\mathbf{B}$, decreasing ϕ and limiting the ESW lifetime. ESWs with larger ϕ may be more unstable effectively reducing the maximum observed ϕ. For example, in the two-dimensional simulations of *Mottez et al.* [1997], the large amplitude ESWs that initially develop are unstable, whereas the lower amplitude ESWs, which develop later, are much more stable.

We now investigate how the magnitude of **B** constrains the amplitudes and length scales of ESWs. *Muschietti et al.* [2000] showed that for $\omega_b > \Omega_{ce}$ ESWs become unstable to instabilities perpendicular to **B**, where ω_b is the angular bounce frequency. In contrast for $\omega_b < \Omega_{ce}$ ESWs remain relatively stable. Multi-dimensional simulations show that once this perpendicular instability develops the ESWs are rapidly dissipated [*Muschietti et al.*, 2000; *Umeda et al.*, 2006; *Wu et al.*, 2010]. Therefore, we propose that $\omega_b < \Omega_{ce}$ is a necessary condition for ESW stability. For small oscillations around the center of the ESW potential [equation (5)]

$$\omega_b \approx \sqrt{\frac{4q_e\phi_{\mathrm{ESW}}}{m_e l_{pp}^2}}. \tag{8}$$

The condition $\omega_b < \Omega_{ce}$ can then be written is

$$\phi_{\mathrm{ESW}} \lesssim \frac{q_e B^2 l_{pp}^2}{4m_e}. \tag{9}$$

Using equation (6) we can rewrite equation (9) as

$$E_{pp} \lesssim \frac{\mathrm{e}^{1/2} q_e B^2 l_{pp}}{m_e} \tag{10}$$

to compare directly with observations. Equations (9) and (10) predict that as B decreases the values of ϕ_{ESW} and E_{pp} decrease, and for a fixed B higher ϕ_{ESW} and E_{pp} can develop for larger l_{pp}. Since l_{pp} tends to increase proportionally with λ_D, higher ϕ_{ESW} and E_{pp} can develop in magnetospheric plasmas, where λ_D is larger than in the magnetosheath.

In Figure 9b we plot E_{pp} versus l_{pp} and $\lambda/2$ for ESWs and electrostatic waves. We also plot equation (10) for $B = 20\,\mathrm{nT}$ and $40\,\mathrm{nT}$, which are close to the mimimum and the mean observed values of B in our survey, respectively. Figure 9b shows that all ESWs satisfy equation (10) for $B = 40\,\mathrm{nT}$, and very few ESWs exceed the threshold for $B = 20\,\mathrm{nT}$. Therefore, the formation of ESWs is consistent with the constraint $\omega_b < \Omega_{ce}$.

We also find that most ESWs have E_{pp} well below the threshold. So we expect these ESWs to remain stable over longer time scales. For weakly magnetized plasmas, in particular, in the magnetosheath, this will restrict the maximum $q_e\phi/k_BT_e$ to values well below the thresholds predicted by *Chen et al.* [2005]. When the plasma is more strongly magnetized, i.e., when the plasma is primarily magnetospheric, $\omega_b < \Omega_{ce}$ is more easily satisfied and the maximum $q_e\phi/k_BT_e$ should be determined by the predictions of *Chen et al.* [2005]. The electrostatic waves are typically observed for smaller $\lambda/2$ and B (Figure 7a), corresponding to magnetosheath plasmas. A large fraction of the electrostatic waves exceed the threshold for $B = 20\,\mathrm{nT}$ and a few exceed the threshold for $B = 40\,\mathrm{nT}$, meaning stable ESWs are unlikely to form from these waves, and equations (9) and (10) apply less strictly to the electrostatic waves. We conclude that at the magnetopause and in the magnetosheath, equation (9) constrains the maximum potentials, such that $q_e\phi/k_BT_e \ll 1$.

5. ESW instabilities

In this section we investigate the instabilities responsible for ESW generation by comparing the wave properties with predictions from linear theory. We consider the following instabilites in detail: the warm bistream instability and the beam-plasma instability. All waves investigated in this paper are consistent with field-aligned electrostatic waves, so we only investigate instabilities that generate electrostatic waves parallel to $\mathbf{B}$. Instabilities exciting electrostatic waves at oblique angles to $\mathbf{B}$ are unlikely to explain the observed waves.

Figure 10 shows representative electron distributions associated with the warm bistream instability, beam-plasma instability, and an electron-ion streaming instability similar to the Buneman instability. The warm bistream instability consists of two counter-

propagating electron distributions, with a decrease in phase-space density between the electron distributions, as shown in Figure 10a. The warm bistream instability is an electron-electron instability, so it can yield a large range of ESW speeds depending on the properties of the counter-propagating electron distributions. The beam-plasma instability (Figure 10b) consists of an electron beam propagating with respect to non-drifting electron and ion distributions. The electron beam has density and temperature below that of the non-drifting electrons. The beam-plasma instability will generate fast ESWs. For the observed ESWs we expect the beam speeds v_b to satisfy $v_b < v_e$ to account for the observed ESW speeds.

Figure 10c shows an example of the electron distribution we expect to excite the electron-ion streaming instability similar to the Buneman instability, described by *Norgren et al.* [2015a]. The distribution consists of dense subthermal beam and non-drifting electrons. Here the beam interacts with the ions (rather than the non-drifting electrons) to generate slower ESWs, with speeds comparable to v_i, potentially accounting for some of the observed waves. This instability is investigated in detail by *Norgren et al.* [2015a], and we refer to their paper for a discussion of the role of this instability in generating ESWs.

5.1. Warm Bistream Instability

In this subsection we investigate the warm bistream instability as a generation mechanism for the observed ESWs, in particular, for the slowest moving ESWs, with speeds well below those expected for electron-ion or beam instabilities. The warm bistream instability is generated by counter-propagating thermal electron populations with comparable densities [*Omura et al.*, 1996; *Mottez et al.*, 1997]. As an example of very slow ESWs we consider the magnetopause crossing observed by C4 on 22 February 2003. An overview is

shown in Figure 11a–11d. C4 was located at $(7.8, 0.2, 8.4)R_E$ (GSM) when EFW's internal burst mode was triggered. The magnetopause crossing occurs at 01:01 UT, indicated by the loss in magnetospheric electrons and increase in magnetosheath electrons, and the increased V, corresponding to magnetosheath particles moving around the magnetopause. There is little evidence of nearby magnetic reconnection: B_z does not reverse direction, and no evidence of ion outflows is observed.

EFW's internal burst mode was triggered where magnetosheath electrons dominate. Figures 11e and 11f show the time series and spectrogram of $\mathbf{E}_{\|}$ over a short time interval. ESWs are observed with $+/-$ polarity, and have similar τ_{pp}. Figure 11h shows the associated frequency-wave number power spectrum, from which we calculate $v \approx 93\,\mathrm{km\,s^{-1}}$ (in the spacecraft frame) and $l_{pp} \approx 6.1\,\lambda_D$. The maximum potential is $\phi \approx 0.14\,\mathrm{V}$, so individual ESWs do not strongly interact with electrons or ions. When the ESWs are observed we calculate $\mathbf{V} \cdot \mathbf{B}/|\mathbf{B}| \sim 60\,\mathrm{km\,s^{-1}}$, so the ESW phase speed in the ion frame is $v' \sim 30\,\mathrm{km\,s^{-1}}$, well below the speeds expected for electron-ion or beam instabilities. Figure 11g shows the electron phase-space density $f_e(E)$ versus electron energy E at pitch angles $\theta = 0°$, 90°, and 180° averaged over the internal burst mode interval. The distribution has a flat-top shape at low E and for $E \gtrsim 100\,\mathrm{eV}$, $f_e(E)$ is largest for $\theta = 0°$ and 180°. This is consistent with saturation of the warm bistream instability after the ESWs form. When the ESWs were observed the ion thermal speed is $v_i \approx 300\,\mathrm{km\,s^{-1}}$, much faster than the ESW speeds in the ion frame. Since the ESWs have very small potentials and v_i is large, ions can transit the ESW without being reflected by the ESW potential. This should enable the ESWs to remain stable. In contrast, low speed ESWs with very large potentials would tend to reflect ions, making the ESWs unstable [*Omura*

et al., 1994; *Drake et al.*, 2003], or accelerating them out of the ion frame [*Eliasson and Shukla*, 2004]. We conclude that these ESWs are stable because the potentials are too small to significantly scatter or reflect ions.

We investigate the warm bistream instability numerically for conditions when magnetosheath electrons dominate by solving the dispersion equation. For a Maxwellian plasma with two electron components and one ion component, the one-dimensional electrostatic dispersion equation is

$$1 + \frac{2\omega_{pi}^2}{k^2 v_i^2}\left[1 + \xi_i Z(\xi_i)\right] + \frac{2\omega_{pe1}^2}{k^2 v_{e1}^2}\left[1 + \xi_{e1} Z(\xi_{e1})\right] + \frac{2\omega_{pe2}^2}{k^2 v_{e2}^2}\left[1 + \xi_{e2} Z(\xi_{e2})\right] = 0, \tag{11}$$

where $\xi_{e1,2} = (\omega - k v_{d1,2})/k v_{e1,2}$, $\xi_i = \omega/k v_i$, Z is the plasma dispersion function, $v_{e1,2}$ and v_i are the electron and ion thermal speeds, $\omega_{pe1,2}$ and ω_{pi} are the electron and ion angular plasma frequencies for each particle distribution, and $v_{d1,2}$ are the drift speeds of the electron distributions. For the electrons we use $n_{e1,2} = 5\,\mathrm{cm}^{-3}$ and $T_{e1,2} = 30\,\mathrm{eV}$. For the ions we use $n_i = 10\,\mathrm{cm}^{-3}$ and $T_i = 200\,\mathrm{eV}$. We allow the relative drift $v_d = v_{d2} - v_{d1}$ between the electron distributions to vary, but keep $v_c = (v_{d1} + v_{d2})/2 = 32.5\,\mathrm{km\,s}^{-1}$ constant in all cases. Figure 12 presents the results of our analyses using equation (11).

We first consider two cases with $v_d = 1.9 v_{e1,2}$ and $3.0 v_{e1,2}$. The electron distributions for the two cases are shown in Figure 12a. The peaks in $f_e(E)$ at $\theta = 0°$ and 180° correspond to v_{d1} and v_{d2}, respectively, and as v_d increases the valley between the distributions deepens. Because v_c is very small compared with v_e, $f_e(E)$ at $\theta = 0°$ and 180° are almost identical. Such distributions are similar to observed magnetosheath distributions, which are often characterized by flat-top distributions and parallel to perpendicular temperature ratio $T_\parallel/T_\perp > 1$, as observed in Figure 11g. Electron distributions averaged over EFW's

internal burst mode interval (not shown) often have $T_\parallel/T_\perp > 1$ and flat-top distributions at low energies, suggestive of a saturated warm bistream instability distribution.

The dispersion relations and growth rates of the unstable modes associated with the two electron distributions are shown in Figure 12b. For $v_d = 1.9v_{e1,2}$ the distribution is unstable to an ion-modified bistream instability. For $v_d = 3.0v_{e1,2}$ the dispersion relation approximately satisfies $\omega = v_c k$ for small k. At higher k the dispersion relation is modified and depends on the ion distribution properties. However, the growth rate is maximal for the linear part of the dispersion relation, and the growth rate is small where the dispersion relation changes at larger k, so the electron-electron instability dominates.

We now allow v_d to vary for constant v_c. In Figure 12c we plot the wave number $k_{\max}$ where the growth rate γ is maximal versus v_d. For the parameters chosen $v_d \gtrsim 1.8v_{e1,2}$ is required for a positive growth rate. At $v_d = 2.02v_{e1,2}$ there is a discontinuity in $k_{\max}$ as the instability changes from the ion-modified bistream instability to the electron-electron warm bistream instability.

Figure 12d shows the frequency $\omega_{\max}$ and growth rate $\gamma_{\max}$ at $k_{\max}$, where γ is maximal. At low v_d, when the ion-modified bistream mode dominates, $\omega_{\max}$ is comparable to ω_{pi}. When the warm bistream mode dominates $\omega_{\max} \sim 0.1\omega_{pi}$. As v_d increases $\gamma_{\max}$ increases but begins to level off at larger v_d. The growth rate of the ion-modified bistream instability is significantly smaller than for the bistream instability. The phase speed $v_{ph} = k_{\max}/\omega_{\max}$ is shown in Figure 12e. The ion-modified bistream mode has v_{ph} comparable to the ion-acoustic speed. As v_d increases and the warm bistream instability dominates v_{ph} decreases and approaches v_c, as expected.

In Figure 12f we can estimate l_{pp}/λ_D for ESWs excited by the instability by assuming the ESW length scale corresponds to the wave number $k_{\max}$, where growth is maximal. To calculate λ_D, we use $v_e^2 = |v_d/2|^2 + v_{e1,2}^2$, which applies for electron beams of equal densities, to calculate the thermal speed of the total electron distribution. The Debye length is then $\lambda_D = v_e/\omega_{pe}\sqrt{2}$. When the ion-modified bistream instability dominates we estimate $l_{pp}/\lambda_D \gtrsim 13$. Based on the results in Figures 5e and 5f, this instability can only account for a small fraction of the observed l_{pp}/λ_D. When the warm bistream instability dominates we predict $6 \lesssim l_{pp}/\lambda_D \lesssim 18$, with l_{pp}/λ_D decreasing as v_d increases. These length scales are consistent with those found for ESWs in simulations of the warm bistream instability [*Goldman et al.*, 1999]. This range of l_{pp}/λ_D overlaps with most of the observed l_{pp}/λ_D in Figures 5e and 5f, and the statistical average $l_{pp} = 8.6\,\lambda_D$. The ESWs in Figure 11 are marginally consistent with Figure 12f, but because the speeds are well below those expected for electron-ion and beam instabilities, we conclude that they could be generated by the warm bistream instability. More generally, for counter-streaming electron distributions v_c can potentially have a large range of values, and could potentially account for ESWs observed over a range of speeds. Indeed, small changes in the counter-streaming electron distributions can lead to large changes in v_{ph}, so very slow ESWs in the ion frame may be rare. We also note that background density fluctuations can modify ESW speeds [*Mandrake et al.*, 2000; *Briand et al.*, 2008], possibly decelerating them. Therefore, the large number of slow ESWs and electrostatic waves in Figures 5 and 6 requires further investigation.

We also model the effect of magnetospheric electrons on the warm bistream instability by including a low-density high-temperature electron distribution in the dispersion equation.

Overall, the changes in the mode properties are negligible. However, the presence of electrons with magnetospheric energies will tend to increase the total electron thermal speed. This will tend to increase λ_D and hence decrease l_{pp}/λ_D. Therefore, it is possible to observe ESWs with smaller l_{pp}/λ_D than calculated in Figure 12f, when magnetospheric electrons are also present. This may account for some of the ESWs with $l_{pp} \lesssim 6\,\lambda_D$ in Figure 5.

The magnitude of v_c determines the total current density J. For the model considered above $J = q_e n_{e1,2}(v_{d1} + v_{d2}) = 2q_e n_{e1,2} v_c$. As v_c and J increase sufficiently current-driven instabilities, such as the Buneman instability, will likely develop. Our interpretation is that the counter-streaming electron populations could have similar properties and small v_c to ensure the current remains small, except where strong currents are expected, for example, at current sheets. The pitch-angle distributions observed with ESWs likely correspond to marginal stability, so it is difficult to reliably predict ESW speeds directly from the observed electron distributions.

In summary, we conclude that the ESWs and electrostatic waves with very small v may be generated by the warm bistream instability for small J. In this case current driven instabilities are unlikely to dominate. Because the warm bistream instability is an electron-electron instability the wave speeds can be large due to non-zero v_c and differences in the counter-streaming electron populations. Therefore, a large range in waves speeds is possible, and can potentially account for a large fraction of the observed speeds in Figures 5 and 6. Similarly, the ESW speeds may change after they develop, for instance, due to fluctuations in the background plasma density. The range of predicted l_{pp}/λ_D is consistent with most of the wave observations in Figure 5. These results suggest that the

warm bistream instability may be responsible for a significant fraction of the observed waves.

5.2. Beam-Plasma Instability

We consider the electrostatic instabilities driven by an electron beam, namely, the beam-plasma instability. Beam-plasma instabilities drive electrostatic waves with $v_{ph} \lesssim v_b$, where v_b is the beam speed. In Figure 5a all wave speeds are below v_e, so for the beam-plasma instability to generate some of the observed ESWs and electrostatic waves $v_b \lesssim v_e$ is required. At Earth's magnetopause subthermal electron beams can be produced by magnetosheath electrons entering the magnetosphere via magnetic reconnection [*Graham et al.*, 2016].

As an example of ESWs generated by the beam-plasma instability, we present ESW observations in the magnetosphere by C4 on 28 May 2004, close to magnetopause boundary. An overview is presented in Figure 13. At the time EFW's internal burst mode was triggered, C4 was located at $(4.1, -11.1, 3.5)\, R_E$ (GSM). Figures 13a and 13b show that $\mathbf{B}$ and n_e change little. However, the electron differential energy flux shifts to lower energies between 01:29 UT and 01:33 UT, corresponding to T_e decreasing. Throughout the internal burst mode interval we observe ESWs propagating both parallel and antiparallel to $\mathbf{B}$. Figures 13d and 13e shows a short time series of $\mathbf{E}_{\|}$ and the associated spectrogram. At this time short time-scale ESWs are observed throughout the time series with $+/-$ polarity. The spectrogram shows that the ESWs have powers at different frequencies, corresponding to different τ_{pp}.

Throughout the region of decreased T_e, evidence for subthermal electron beams is observed, propagating parallel and antiparallel to $\mathbf{B}$. Figure 13f shows $f_e(E)$ when the

parallel propagating ESWs in Figures 13d and 13e are observed. For energies below $\sim 100\,\mathrm{eV}$ an enhancement of electrons propagating parallel to $\mathbf{B}$ is observed, suggestive of a thermalized beam. Overplotted is our fit to the data using a sum of bi-Maxwellian distribution functions. The fitted distribution consists of a beam of subthermal electrons propagating parallel to $\mathbf{B}$, another electron population drifting antiparallel to $\mathbf{B}$, and a thermal background of magnetospheric electrons. For the fit we reduce the beam temperature to correspond more closely to a distribution before the instability develops and the beam is thermalized. The beam density is approximately 12% of the total electron density, based on the fit to the data.

In Figure 13g we plot the frequency-wave number power spectrum for the ESWs in Figure 13d. Two ESW populations are observed with $v \approx 3000\,\mathrm{km\,s^{-1}}$ and $800\,\mathrm{km\,s^{-1}}$. At this time $\mathbf{V}$ is small compared with the ESW speeds, so Doppler shifts are negligible. The corresponding l_{pp} of the faster and slower ESWs are $4.9\,\lambda_D$ and $5.1\,\lambda_D$, respectively. The maximum potentials are $\phi \approx 2.8\,\mathrm{V}$ and $\phi \approx 0.82\,\mathrm{V}$ for the faster and slower ESWs, respectively, corresponding to $v_T \approx 1000\,\mathrm{km\,s^{-1}}$ and $v_T \approx 500\,\mathrm{km\,s^{-1}}$. Therefore, the ranges of trapped electron speeds ($v \pm v_T$) do not overlap, meaning the faster ESWs can pass the slower ESWs without coalescence.

The fitted $f_e(E)$ in Figure 13f is unstable to the electrostatic beam mode. The dispersion relation and growth rate of the beam mode is found using WHAMP for the fitted electron distribution, and are overplotted in Figure 13g. (For higher beam temperatures the beam mode is stabilized and no positive growth is observed.) For the beam mode we predict $v_{ph} \approx 2800\,\mathrm{km\,s^{-1}}$, in good agreement with the faster ESWs. Moreover, we predict positive growth for $0 \leq k_{\parallel} \leq 3.4 \times 10^{-3}\,\mathrm{m^{-1}}$, in agreement with the observed range of $k_{\parallel}$ with the

largest power. The growth rate peaks at $k_{\parallel} = 1.9 \times 10^{-3}\,\mathrm{m}^{-1}$, from which we estimate $l_{pp} = \pi/k_{\parallel} = 8.4\,\lambda_D$, comparable to but larger than the observed $l_{pp} \approx 4.9\,\lambda_D$. We conclude that the faster ESWs are consistent with generation by the beam-plasma instability.

The slower ESWs have speeds comparable to the ion thermal speed $v_i \approx 500\,\mathrm{km\,s}^{-1}$ and may correspond to an electron-ion instability. If the beam density is sufficiently large the electron-ion streaming instability can be excited between the beam electrons and background ions, which could account for the observed speed of the slower ESWs [*Norgren et al.*, 2015a].

More generally, we conclude that the faster ESWs observed in Figures 5a and 6a are consistent with generation by the beam-plasma instability. In Figure 5a the fastest moving ESWs are typically observed for larger T_e, corresponding to a higher proportion of magnetospheric electrons. Our interpretation is that close to the magnetopause boundary, magnetosheath electrons entering the magnetosphere form the subthermal beams, which excite ESWs via the beam-plasma instability [*Graham et al.*, 2016]. Electron beams are also possible in the magnetosheath and may generate ESWs there as well.

6. Discussion

At the magnetopause the largest amplitude ESWs had $E_{pp} \sim 50\,\mathrm{mV\,m}^{-1}$ and a maximum $\phi \sim 100\,\mathrm{V}$. However, in other near-Earth regions, such as the near magnetotail and auroral zones, ESWs have been observed with E_{pp} of several hundred $\mathrm{mV\,m}^{-1}$ and ϕ exceeding 1 kV, corresponding to maximum $q_e\phi/k_BT_e \sim 1$ [*Ergun et al.*, 1998b; *Andersson et al.*, 2009; *Tao et al.*, 2011]. This can be explained by the constraints of equations (9) and (10), which predict that the maximum E_{pp} and ϕ are constrained by B and l_{pp}. For example, in Earth's near magnetotail B is often comparable to the values of B at the

magnetopause; however, n_e is typically much smaller and T_e is larger in the magnetotail. Assuming l_{pp}/λ_D does not change significantly for ESWs at the magnetopause and magnetotail, then based on equation (10), $E_{pp} \propto \lambda_D$ or equivalently $E_{pp} \propto \sqrt{T_e/n_e}$. This means that larger values of E_{pp} are allowed in the magnetotail. Based on equation (9), $\phi \propto T_e/n_e$, so larger ϕ are also allowed. Moreover, $q_e\phi/k_BT_e \propto 1/n_e$, so as the density decreases a higher proportion of the background electrons can become trapped in ESW potentials for constant B. In the auroral zone, B is much larger than values at the magnetopause and magnetotail, such that $\Omega_{ce} \gg \omega_{pe}$. In this case ϕ is not limited by B, but are limited by the constraints in *Chen et al.* [2005]. For typical solar wind conditions we would expect small amplitude ESWs, as was found in *Malaspina et al.* [2013]. However, some ESW reported near the bowshock have very large amplitudes [*Bale et al.*, 1998], which seem to exceed these constraints. We conclude that B and the ESW length scales constrain ϕ at the magnetopause to smaller values than can be observed in the near magnetotail and auroral zones. The smaller values of ϕ for ESWs at the magnetopause allows ESWs with distinct speeds to coexist without coalescing.

In this paper we have compared the speeds and length scales of ESWs with predictions from linear theory, with very good agreement. Statistically, there is little difference in the typical speeds and length scales (normalized to λ_D) of ESWs and electrostatic waves, which suggests the same instabilities may be responsible for both ESWs and field-aligned electrostatic waves. Similarly, there is little change in the dispersion relation as the waveforms of electrostatic waves become nonlinear and form ESWs. The frequency-wave number spectra of both ESWs and electrostatic waves are generally well modeled by the linear dispersion relation [equation (4)]. However, simulations are required to determine to

what degree the dispersion relation and mode properties change as they become nonlinear for typical magnetopause and magnetosheath conditions. For example, the length scales may increase as ESWs of comparable speeds coalesce [*Omura et al.*, 1994].

For the ranges of T_e and n_e at the magnetopause and in the magnetosheath, EFW's sampling rate is too small to resolve waves with $v \gtrsim v_e$. Future work is required to investigate and characterize ESWs and electrostatic waves with speeds near or above v_e. At the magnetopause, bump-on-tail or lower-hybrid instabilities could lead to the development of fast ESWs [*Omura et al.*, 1996; *Che et al.*, 2010]. Both instabilities are possible at the magnetopause, especially if magnetic reconnection is occurring. Therefore, higher time resolution measurements are required to characterize ESWs generated by these instabilities. *Pickett et al.* [2005] found ESWs in the magnetosheath with time scales < 0.1 ms using Cluster's Wideband Data (WBD) plasma wave receiver, which suggests that faster ESWs are present, but undetected by EFW's internal burst mode, in some cases.

Magnetic reconnection may play an important role in the generation of many of the observed ESWs and electrostatic waves. Although ESWs and electrostatic waves are also observed in the unperturbed magnetosheath and at the flanks of the magnetopause, where reconnection is unlikely. Numerous observations and simulations have shown that ESWs are generated in the separatrices of magnetic reconnection [*Drake et al.*, 2003; *Cattell et al.*, 2005; *Divin et al.*, 2012; *Li et al.*, 2014; *Fujimoto*, 2014; *Graham et al.*, 2015]. Observations and simulations show that ESWs develop near the electron diffusion region [*Goldman et al.*, 2008; *Tang et al.*, 2013; *Jara-Almonte et al.*, 2014]. In these regions electron beams, bistreaming electrons, and strong currents are observed potentially lead-

ing to the excitation of the beam, bistream, and electron-ion instabilities, respectively. Many of the examples presented in this paper show evidence of magnetic reconnection. In particular, ion outflows and mixing of magnetospheric and magnetosheath electrons are observed. Mixing of the two plasmas occurs in the outflow regions of magnetic reconnection and separatrices. In this paper the wave events associated with reconnection are primarily observed in the outflow and separatrix regions, similar to *Graham et al.* [2015]. Therefore, the waves are observed outside the diffusion region, so they likely do not influence ongoing reconnection at the magnetopause.

The lack of field measurements along the spin axis means that ESWs and electrostatic waves at the magnetopause near the subsolar point are under-represented. Near this region, particularly on the magnetospheric side of the boundary, the component of **B** along the spin axis is too large to characterize ESWs and electrostatic waves. This region is of particular interest to investigate the diffusion region and separatrices of asymmetric magnetic reconnection. In particular, the observation of both slow and faster, but still subthermal, ESWs and electrostatic waves means that ESWs can dissipate strong currents and couple different electron populations. The role of ESWs and electrostatic waves could be crucial for asymmetric reconnection. With the magnetospheric Multiscale (MMS) mission we will be able to measure the electric fields in three dimensions, providing much better coverage of the magnetopause. In particular, ESWs can be observed and characterized at the subsolar point, where asymmetric reconnection occurs. Future work is required to determine the role of ESWs and electrostatic waves in the reconnection diffusion region.

7. Conclusion

In this paper we have investigated the characteristics of ESWs and field-aligned electrostatic waves near Earth's magnetopause and in the magnetosheath. Both types of waves are frequently observed. We have used cross-spectral analyses to determine the speeds, length scales, and maximum potentials of the waves. The key results are as follows:

(1) The phase speeds of electrostatic solitary waves (ESWs) and electrostatic waves span approximately two orders of magnitude for similar plasma conditions, ranging from almost stationary speeds in the ion frame to speeds comparable to, but smaller than, the electron thermal speed. This suggests that multiple instabilities are responsible for the observed waves.

(2) The length scales tend to increase linearly with λ_D. The range of l_{pp}/λ_D is much smaller than the range of observed speeds. For ESWs the average peak-to-peak length is $9\,\lambda_D$. Statistically, there is little change between the length scales of ESWs and field-aligned electrostatic waves, suggesting that the same instabilities may be responsible for both types of waves and the length scales do not change significantly as linear waves evolve into the nonlinear ESWs.

(3) ESWs are more probable compared with electrostatic waves for low ω_{pe}/Ω_{ce}, i.e., when the plasma becomes more strongly magnetized. For less magnetized plasmas electrostatic waves are more probable, and for $\omega_{pi} \gtrsim \Omega_{ce}$ no ESWs were observed in our survey. This suggests that when the plasma becomes too weakly magnetized ESWs are no longer stable. Similarly, ESWs are only observed when $\omega_b < \Omega_{ce}$, consistent with multi-dimensional simulations, which constrains the maximum allowable field strengths and potentials.

(4) The maximum potentials associated with ESWs are typically $q_e\phi/k_BT_e \sim 0.01$, i.e., small compared with the thermal electron energy. The observed values of $q_e\phi/k_BT_e$ and l_{pp}/λ_D (and $\lambda/2\lambda_D$ for electrostatic waves) are consistent with the requirements for stable ESWs predicted by *Chen et al.* [2005]. Large numbers of ESWs and extended electrostatic waves are often observed, which suggests particle scattering and isotropization by these waves can be significant, resulting in particle heating and plasma resistivity.

(5) The ESWs and electrostatic waves are consistent with those generated by the beam-plasma instability, the warm bistream instability, and electron-ion instabilities. These instabilities account for the range of observed phase speeds, and the typical observed length scales. The fact that a large range of wave speeds are observed indicates that particle scattering can occur over a wide range of energies.

(6) Waves with distinct speeds are often observed together or are closely separated [*Graham et al.*, 2015]. This indicates that the plasma can be unstable to multiple instabilities simultaneously. The ESW potentials are often sufficiently small that the ranges of trapped electron speeds do not overlap for ESWs with distinct speeds. This means that ESWs with distinct speeds can pass through each other without coalescence.

The observed ESWs and electrostatic waves can couple different electron populations. The slower waves can couple electron and ions, which can introduce effective collisions and resistivety, and dissipate strong currents. Therefore, they could play a significant role in magnetic reconnection at the magnetopause.

Acknowledgments. We thank the ESA Cluster Science Archive team and the Cluster PI teams for data access and support. The data used in this paper were provided by the

Cluster Science Archive (http://www.cosmos.esa.int/web/csa). This work was supported by the Swedish National Space Board, Grant Nos. 128/11:2 and 77/13.

References

Andersson, L., et al. (2009), New features of electron phase space holes observed by the THEMIS mission, *Phys. Rev. Lett.*, *102*, 225,004, doi:10.1103/PhysRevLett.102.225004.

Bale, S. D., P. J. Kellogg, D. E. Larson, R. P. Lin, K. Goetz, and R. P. Lepping (1998), Bipolar electrostatic structures in the shock transition region: Evidence of electron phase space holes, *Geophys. Res. Lett.*, *25*, 2929, doi:10.1029/98GL02111.

Balogh, A., et al. (2001), The Cluster Magnetic Field Investigation: overview of in-flight performance and initial results, *Ann. Geophys.*, *19*, 1207, doi:10.5194/angeo-19-1207-2001.

Behlke, R., M. André, S. D. Bale, J. S. Pickett, C. A. Cattell, E. A. Lucek, and A. Balogh (2004), Solitary structures associated with short large-amplitude magnetic structures (SLAMS) upstream of the Earth's quasi-parallel bow shock, *Geophys. Res. Lett.*, *31*, L16,805, doi:10.1029/2004GL019524.

Bernstein, I. B., J. M. Greene, and M. D. Kruskal (1957), Exact nonlinear plasma oscillations, *Phys. Rev.*, *108*, 546, doi:10.1103/PhysRev.108.546.

Berthomier, M., L. Muschietti, J. W. Bonnell, I. Roth, and C. W. Carlson (2002), Interaction between electrostatic whistlers and electron holes in the auroral region, *J. Geophys. Res.*, *107*, 1463, doi:10.1029/2002JA009303.

Briand, C., A. Mangeney, and F. Califano (2008), Coherent electric structures: Vlasov-Ampere simulations and observational consequences, *J. Geophys. Res.*, *113*, A07,219,

doi:10.1029/2007JA012992.

Buneman, O. (1959), Dissipation of currents in ionized media, *Phys. Rev.*, *115*, 503, doi: 10.1103/PhysRev.115.503.

Cattell, C., J. Crumley, J. Dombeck, J. Wygant, and F. S. Mozer (2002), Polar observations of solitary waves at the earth's magnetopause, *Geophys. Res. Lett.*, *29*, 1065, doi:10.1029/2001GL014046.

Cattell, C., C. Neiman, J. Dombeck, J. Crumley, J. Wygant, C. A. Kletzing, W. K. Peterson, F. S. Mozer, and M. André (2003), Large amplitude solitary waves in and near the Earth's magnetosphere, magnetopause and bow shock: Polar and Cluster observations, *Nonlinear Processes in Geophysics*, *10*, 13, doi:10.5194/npg-10-13-2003.

Cattell, C., et al. (2005), Cluster observations of electron holes in association with magnetotail reconnection and comparison to simulations, *J. Geophys. Res.*, *110*, A01,211, doi:10.1029/2004JA010519.

Che, H., J. F. Drake, M. Swisdak, and P. H. Yoon (2009), Nonlinear development of streaming instabilities in strongly magnetized plasma, *Phys. Rev. Lett.*, *102*, 145,004, doi:10.1103/PhysRevLett.102.145004.

Che, H., J. F. Drake, M. Swisdak, and P. H. Yoon (2010), Electron holes and heating in the reconnection dissipation region, *Geophys. Res. Lett.*, *37*, L11,105, doi: 10.1029/2010GL043608.

Chen, L.-J., J. Pickett, P. Kintner, J. Franz, and D. Gurnett (2005), On the width-amplitude inequality of electron phase space holes, *J. Geophys. Res.*, *110*, A09,211, doi:10.1029/2005JA011087.

Divin, A., G. Lapenta, S. Markidis, D. L. Newman, and M. V. Goldman (2012), Numerical simulations of separatrix instabilities in collisionless magnetic reconnection, *Phys. Plasmas*, *19*, 042,110, doi:10.1063/1.3698621.

Dombeck, J., C. Cattell, J. Crumley, W. K. Peterson, H. L. Collin, and C. Kletzing (2001), Observed trends in auroral zone ion mode solitary wave structure characteristics using data from Polar, *J. Geophys. Res.*, *106*, 19,013, doi:10.1029/2000JA000355.

Drake, J. F., M. Swisdak, C. Cattell, M. A. Shay, B. N. Rogers, and A. Zeiler (2003), Formation of electron holes and particle energization during magnetic reconnection, *Science*, *299*, 873, doi:10.1126/science.1080333.

Dudok de Wit, T., V. V. Krasnosel'skikh, S. D. Bale, M. W. Dunlop, H. Lühr, S. J. Schwartz, and L. J. C. Woolliscroft (1995), Determination of dispersion relations in quasi-stationary plasma turbulence using dual satellite data, *Geophys. Res. Lett.*, *22*, 2653, doi:10.1029/95GL02543.

Dyrud, L. P., and M. M. Oppenheim (2006), Electron holes, ion waves, and anomalous resistivity in space plasmas, *J. Geophys. Res.*, *111*, A01,302, doi:10.1029/2004JA010482.

Eliasson, B., and P. K. Shukla (2004), Dynamics of electron holes in an electron-oxygen-ion plasma, *Phys. Rev. Lett.*, *93*, 045,001, doi:10.1103/PhysRevLett.93.045001.

Ergun, R. E., et al. (1998a), FAST satellite observations of large-amplitude solitary structures, *Geophys. Res. Lett.*, *25*, 2041, doi:10.1029/98GL00636.

Ergun, R. E., C. W. Carlson, J. P. McFadden, F. S. Mozer, L. Muschietti, I. Roth, and R. J. Strangeway (1998b), Debye-scale plasma structures associated with magnetic-field-aligned electric fields, *Phys. Rev. Lett.*, *81*, 826, doi:10.1103/PhysRevLett.81.826.

Escoubet, C. P., M. Fehringer, and M. Goldstein (2001), Introduction: The Cluster mission, *Ann. Geophys.*, *19*, 1197, doi:10.5194/angeo-19-1197-2001.

Fox, W., M. Porkolab, J. Egedal, N. Katz, and A. Le (2008), Laboratory observations of electron phase-space holes during magnetic reconnectio, *Phys. Rev. Lett.*, *101*, 255,003, doi:10.1103/PhysRevLett.101.255003.

Franz, J. R., P. M. Kintner, and J. S. Pickett (1998), POLAR observations of coherent electric field structures, *Geophys. Res. Lett.*, *25*, 1277, doi:10.1029/98GL50870.

Franz, J. R., P. M. Kintner, C. E. Seyler, J. S. Pickett, and J. D. Scudder (2000), On the perpendicular scale of electron phase-space holes, *Geophys. Res. Lett.*, *27*, 169, doi:10.1029/1999GL010733.

Franz, J. R., P. M. Kintner, J. S. Pickett, and L.-J. Chen (2005), Properties of small-amplitude electron phase-space holes observed by Polar, *J. Geophys. Res.*, *110*, A09,212, doi:10.1029/2005JA011095.

Fujimoto, K. (2014), Wave activities in separatrix regions of magnetic reconnection, *Geophys. Res. Lett.*, *41*, 2721, doi:10.1002/2014GL059893.

Fujimoto, M., I. Shinohara, and H. Kojima (2011), Reconnection and waves: A review with a perspective, *Space Sci. Rev.*, *160*, 123, doi:10.1007/s11214-011-9807-7.

Goldman, M. V., M. M. Oppenheim, and D. L. Newman (1999), Nonlinear two-stream instabilities as an explanation for auroral bipolar wave structures, *Geophys. Res. Lett.*, *26*, 1821, doi:10.1029/1999GL900435.

Goldman, M. V., D. L. Newman, and P. Pritchett (2008), Vlasov simulations of electron holes driven by particle distributions for PIC reconnection simulations with a guide field, *Geophys. Res. Lett.*, *35*, L22,109, doi:10.1029/2008GL035608.

Graham, D. B., Y. V. Khotyaintsev, A. Vaivads, and M. André (2015), Electrostatic solitary waves with distinct speeds associated with asymmetric reconnection, *Geophys. Res. Lett.*, *42*, 215, doi:10.1002/2014GL062538.

Graham, D. B., A. Vaivads, Y. V. Khotyaintsev, and M. André (2016), Whistler emission in the separatrix regions of asymmetric reconnection, *J. Geophys. Res.*, *121*, doi:10.1002/2015JA021239.

Gustafsson, G., et al. (1997), The Electric Field and Wave experiment for the Cluster Mission, *Space Sci. Rev.*, *79*, 137, doi:10.1023/A:1004975108657.

Jara-Almonte, J., W. Daughton, and H. Ji (2014), Debye scale turbulence within the electron diffusion layer during magnetic reconnection, *Phys. Plasmas*, *21*, 032,114, doi:10.1063/1.4867868.

Johnstone, A. D., et al. (1997), Peace: A Plasma Electron and Current Experiment, *Space Sci. Rev.*, *79*, 351, doi:10.1023/A:1004938001388.

Khotyaintsev, Y., P.-A. Lindqvist, A. Eriksson, and M. André (2010a), The EFW data in the CAA, in *The Cluster Active Archive, Studying the Earth's Space Plasma Environment*, p. 97, Springer.

Khotyaintsev, Y. V., A. Vaivads, M. André, M. Fujimoto, A. Retinò, and C. J. Owen (2010b), Observations of slow electron holes at a magnetic reconnection site, *Phys. Rev. Lett.*, *105*, 165,002, doi:10.1103/PhysRevLett.105.165002.

Kojima, H., Y. Omura, H. Matsumoto, K. Miyaguti, and T. Mukai (1999), Characteristics of electrostatic solitary waves observed in the plasma sheet boundary: Statistical analyses, *Nonlinear Processes in Geophysics*, *6*, 179, doi:10.5194/npg-6-179-1999.

Lapenta, G., S. Markidis, A. Divin, M. V. Goldman, and D. L. Newman (2011), Bipolar electric field signatures of reconnection separatrices for a hydrogen plasma at realistic guide fields, *Geophys. Res. Lett.*, *38*, L17,104, doi:10.1029/2011GL048572.

Lefebvre, B., L.-J. Chen, W. Gekelman, P. Kintner, J. Pickett, P. Pribyl, and S. Vincena (2011), Debye-scale solitary structures measured in a beam-plasma laboratory experiment, *Nonlinear Processes in Geophysics*, *18*, 41, doi:10.5194/npg-18-41-2011.

Li, S. Y., Y. Omura, B. Lembège, X. H. Deng, H. Kojima, Y. Saito, and S. F. Zhang (2014), Geotail observation of counter directed ESWs associated with the separatrix of magnetic reconnection in the near-Earth magnetotail, *J. Geophys. Res.*, *119*, 202, doi:10.1002/2013JA018920.

Lu, Q. M., B. Lembege, J. B. Tao, and S. Wang (2008), Perpendicular electric field in two-dimensional electron phase-holes: A parameter study, *J. Geophys. Res.*, *113*, A11,219, doi:10.1029/2008JA013693.

Malaspina, D. M., D. L. Newman, L. B. Willson III, K. Goetz, P. J. Kellogg, and K. Kerstin (2013), Electrostatic solitary waves in the solar wind: Evidence for instability at solar wind current sheets, *J. Geophys. Res.*, *118*, 591, doi:10.1002/jgra.50102.

Mandrake, L., P. L. Pritchett, and F. V. Coroniti (2000), Electron beam generated solitary structures in a nonuniform plasma system, *Geophys. Res. Lett.*, *27*, 2869, doi:10.1029/2000GL003785.

Mangeney, A., et al. (1999), WIND observations of coherent electrostatic waves in the solar wind, *Ann. Geophys.*, *17*, 307, doi:10.1007/s00585-999-0307-y.

Matsukiyo, S., and M. Scholer (2006), On microinstabilities in the foot of high Mach number perpendicular shocks, *J. Geophys. Res.*, *111*, A06,104, doi:10.1029/2005JA011409.

Matsumoto, H., H. Kojima, T. Miyatake, Y. Omura, M. Okada, I. Nagano, and M. Tsutsui (1994), Electrostatic solitary waves (ESW) in the magnetotail: BEN wave forms observed by GEOTAIL, *Geophys. Res. Lett.*, *21*, 2915, doi:10.1029/94GL01284.

Matsumoto, H., X. H. Deng, H. Kojima, and R. R. Anderson (2003), Observation of electrostatic solitary waves associated with reconnection on the dayside magnetopause boundary, *Geophys. Res. Lett.*, *30*, 59–1, doi:10.1029/2002GL016319.

Miyake, T., Y. Omura, H. Matsumoto, and H. Kojima (1998), Two-dimensional computer simulations of electrostatic solitary waves observed by Geotail spacecraft, *J. Geophys. Res.*, *103*, 11,841, doi:10.1029/98JA00760.

Mottez, F., S. Perraut, and A. Roux (1997), Coherent structures in the magnetotail triggered by counter streaming electron beams, *J. Geophys. Res.*, *102*, 11,399, doi:10.1029/97JA00385.

Mozer, F. S., O. V. Agapitov, A. Artemyev, J. F. Drake, V. Krasnoselskikh, S. Lejosne, and I. Vasko (2015), Time domain structures: What they are, what they do, and how they are made, *Geophys. Res. Lett.*, *42*, 3627, doi:10.1002/2015GL063946.

Muschietti, L., I. Roth, C. W. Carlson, and R. E. Ergun (2000), Transverse instability of magnetized electron holes, *Phys. Rev. Lett.*, *85*, 94, doi:10.1103/PhysRevLett.85.94.

Norgren, C., M. André, D. B. Graham, Y. V. Khotyaintsev, and A. Vaivads (2015a), Slow electron holes in multicomponent plasmas, *Geophys. Res. Lett.*, *42*, 7264, doi:10.1002/2015GL065390.

Norgren, C., M. André, A. Vaivads, and Y. V. Khotyaintsev (2015b), Slow electron phase space holes: Magnetotail observations, *Geophys. Res. Lett.*, *42*, 1654, doi:10.1002/2015GL063218.

Øieroset, M., D. Sundkvist, C. C. Chaston, T. D. Phan, F. S. Mozer, J. P. McFadden, V. Angelopoulos, L. Andersson, and J. P. Eastwood (2014), Observations of plasma waves in the colliding jet region of a magnetic flux rope flanked by two active X lines at the sub solar magnetopause, *J. Geophys. Res.*, *119*, 6256, doi:10.1002/2014JA020124.

Omura, Y., H. Kojima, and H. Matsumoto (1994), Computer simulation of electrostatic solitary waves: A nonlinear model of broadband electrostatic noise, *Geophys. Res. Lett.*, *21*, 2923, doi:10.1029/94GL01605.

Omura, Y., H. Matsumoto, T. Miyake, and H. Kojima (1996), Electron beam instabilities as generation mechanism of electrostatic solitary waves in the magnetotail, *J. Geophys. Res.*, *101*, 2685, doi:10.1029/95JA03145.

Oppenheim, M. M., G. Vetoulis, D. L. Newman, and M. V. Goldman (2001), Evolution of electron phase-space holes in 3D, *Geophys. Res. Lett.*, *28*, 1891, doi: 10.1029/2000GL012383.

Pickett, J. S., L.-J. Chen, S. W. Kahlar, O. Santolík, D. A. Gurnett, B. T. Tsurutani, and A. Balogh (2004), Isolated electrostatic structures observed throughout the Cluster orbit: relationship to magnetic field strength, *Ann. Geophys.*, *22*, 2515, doi:10.5194/angeo-22-2515-2004.

Pickett, J. S., et al. (2005), On the generation of solitary waves observed by Cluster in the near-Earth magnetosheath, *Nonlinear Processes in Geophysics*, *12*, 181, doi: 10.5194/npg-12-181-2005.

Pickett, J. S., et al. (2008), Furthering our understanding of electrostatic solitary waves through Cluster multispacecraft observations and theory, *Adv. Space. Phys.*, *41*, 1666, doi:10.1016/j.asr.2007.05.064.

Pritchett, P. L. (2005), Onset and saturation of guide-field magnetic reconnection, *Phys. Plasmas*, *12*, 062,301, doi:10.1063/1.1914309.

Reme, H., et al. (1997), The Cluster Ion Spectrometry (CIS) Experiment, *Space Sci. Rev.*, *79*, 303, doi:10.1023/A:1004929816409.

Shin, K., H. Kojima, H. Matsumoto, and T. Mukai (2008), Characteristics of electrostatic solitary waves in the earth's foreshock region: Geotail observations, *J. Geophys. Res.*, *113*, A03,101, doi:10.1029/2007JA012344.

Singh, N., S. M. Loo, and E. Wells (2001), Electron hole structure and its stability depending on plasma magnetization, *J. Geophys. Res.*, *106*, 21,183, doi:10.1029/2001JA900056.

Tang, X., C. Cattell, J. Dombeck, L. Dai, L. B. Wilson III, A. Breneman, and A. Hupach (2013), THEMIS observations of the magnetopause electron diffusion region: Large amplitude waves and heated electrons, *Geophys. Res. Lett.*, *40*, 2884, doi:10.1002/grl.50565.

Tao, J. B., et al. (2011), A model of electromagnetic electron phase-space holes and its application, *J. Geophys. Res.*, *116*, A11,213, doi:10.1029/2010JA016054.

Umeda, T., Y. Omura, H. Matsumoto, and H. Usui (2002), Formation of electrostatic solitary waves in space plasmas: Particle simulations with open boundary conditions, *J. Geophys. Res.*, *107*, 1449, doi:10.1029/2001JA000286.

Umeda, T., Y. Omura, T. Miyake, H. Matsumoto, and M. Ashour-Abdalla (2006), Nonlinear evolution of the two-stream instability: Two-dimensional particle simulations, *J. Geophys. Res.*, *111*, A10,206, doi:10.1029/2006JA011762.

Wu, M., Q. Lu, C. Huang, and S. Wang (2010), Transverse instability and perpendicular electric field in two-dimensional electron phase-space holes, *J. Geophys. Res.*, *115*, A10,245, doi:10.1029/2009JA015235.

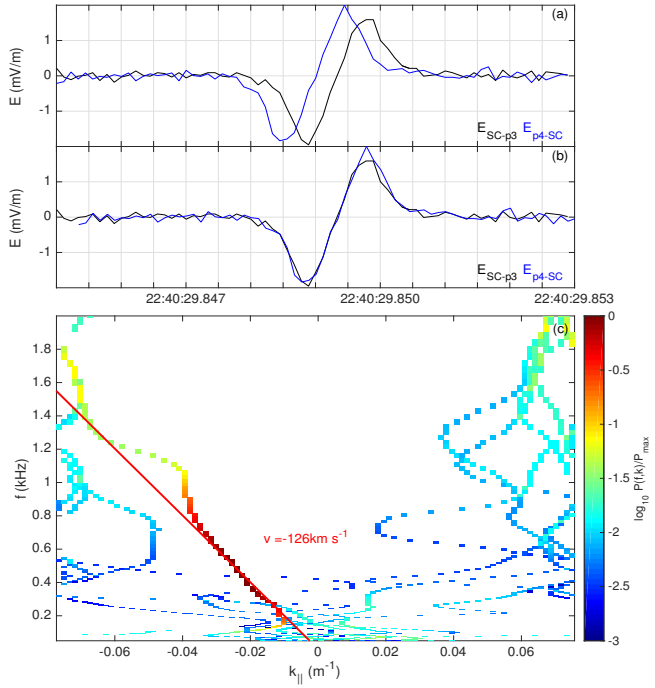

Figure 1. ESW and the associated frequency-wave number power spectrum. (a) $\mathbf{E}_{\mathrm{SC-p3}}$ and $\mathbf{E}_{\mathrm{p4-SC}}$. (b) $\mathbf{E}_{\mathrm{SC-p3}}$, and $\mathbf{E}_{\mathrm{p4-SC}}$ time shifted by 0.34 ms, corresponding to a speed of 122 km s^{-1} antiparallel to $\mathbf{B}$. (c) Frequency-wave number power spectrum obtained from $\mathbf{E}_{\mathrm{SC-p3}}$ and $\mathbf{E}_{\mathrm{p4-SC}}$.

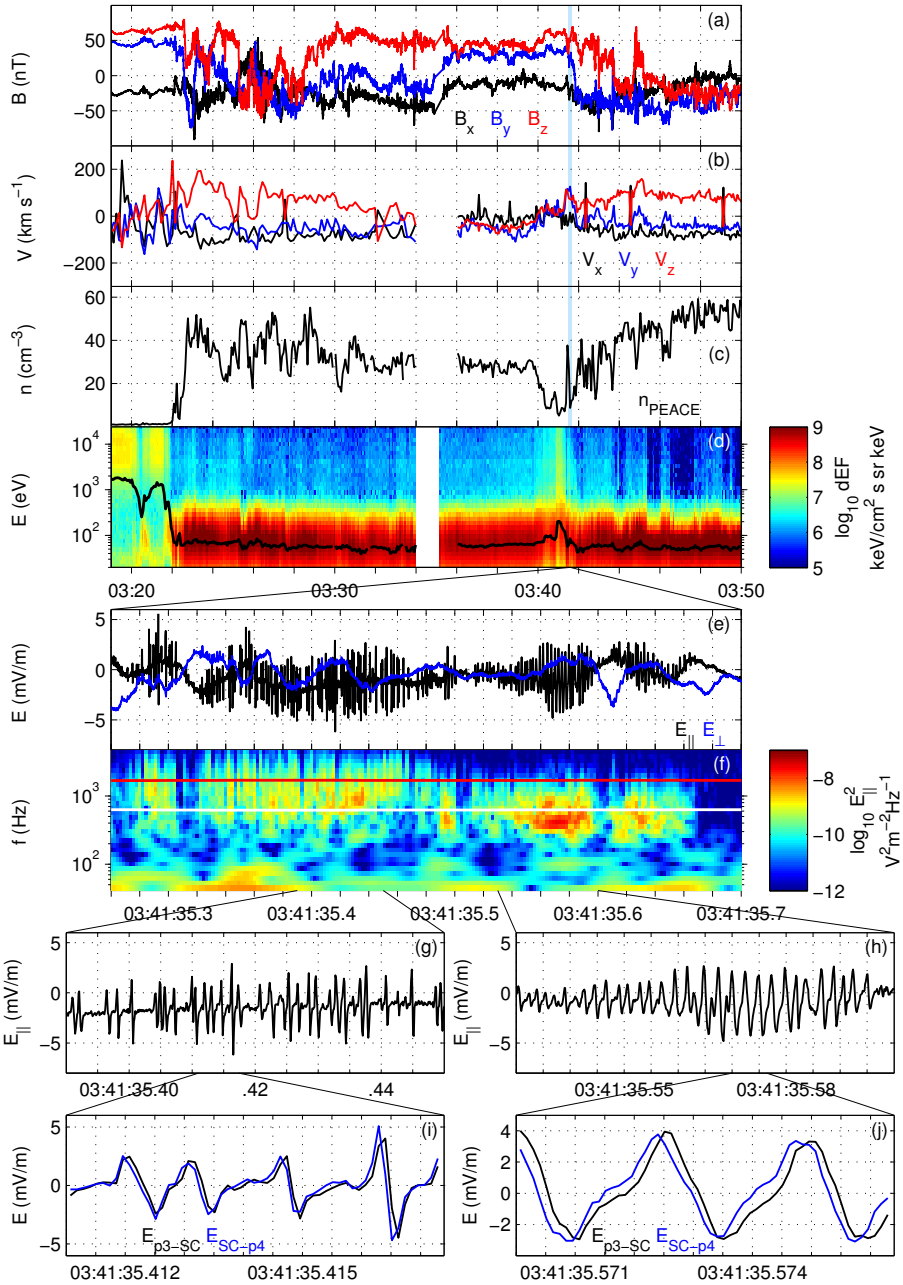

Figure 2. Magnetopause crossing observed by C4 on 28 April 2006. (a) **B** (GSM), (b) **V** (GSM), (c) n_e, and (d) electron differential energy flux (the black line is T_e). The blue shading in (a)–(c) is EFW's internal burst mode interval. (e) $\mathbf{E}_{\parallel}$ (black) and $\mathbf{E}_{\perp}$ (blue) and (f) the $\mathbf{E}_{\parallel}$ spectrogram (the red and white lines are f_{ce} and f_{pi}). (g) and (h) $\mathbf{E}_{\parallel}$ for ESWs and electrostatic waves, respectively. (i) and (j) $\mathbf{E}_{\mathrm{p3-SC}}$ and $\mathbf{E}_{\mathrm{SC-p4}}$ for ESWs and electrostatic waves, respectively.

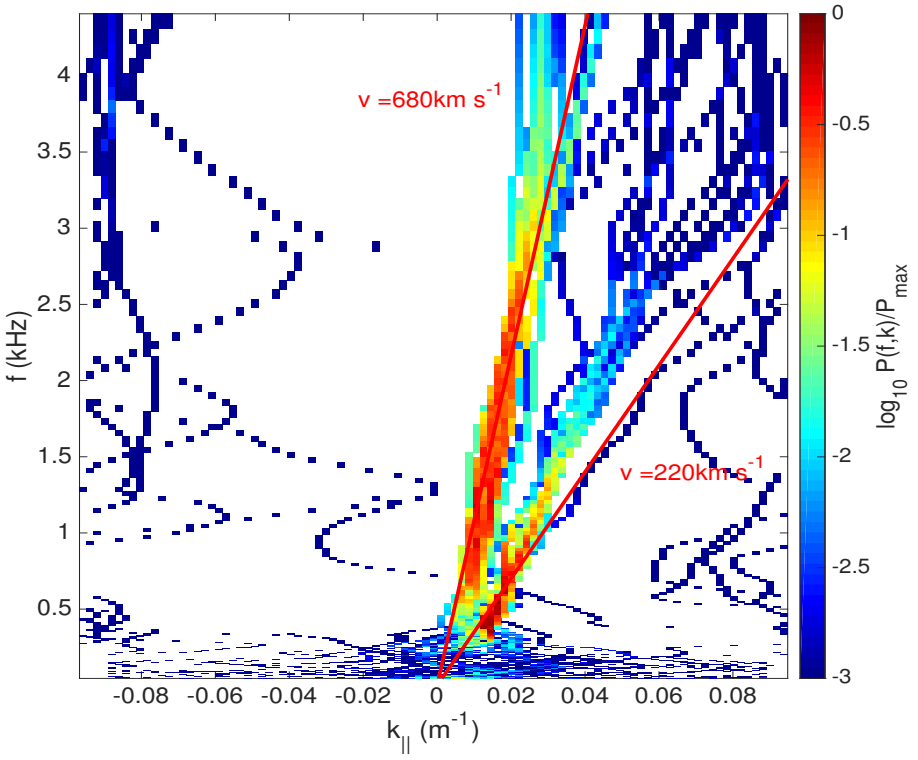

Figure 3. Frequency-wave number power spectrum obtained from $\mathbf{E}_{\mathrm{p3-SC}}$ and $\mathbf{E}_{\mathrm{SC-p4}}$ for the waves in Figure 2e. Overplotted in red are the linear dispersion relation fits to the data.

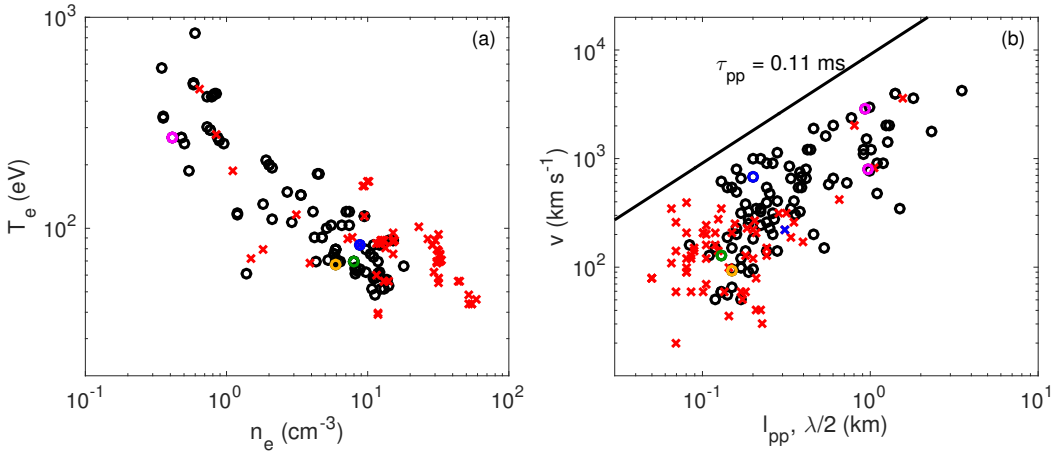

Figure 4. (a) Electron temperature T_e versus electron number density n_e for each wave event. (b) Wave speed v versus peak-to-peak lengths l_{pp} and half wavelengths $\lambda/2$ for ESWs (black circles) and electrostatic waves (red crosses), respectively. The solid line corresponds to $\tau_{pp} = 0.11$ ms. The waves in Figures 1, 2, 11, and 13 are represented by the green, blue, orange, and magenta symbols, respectively.

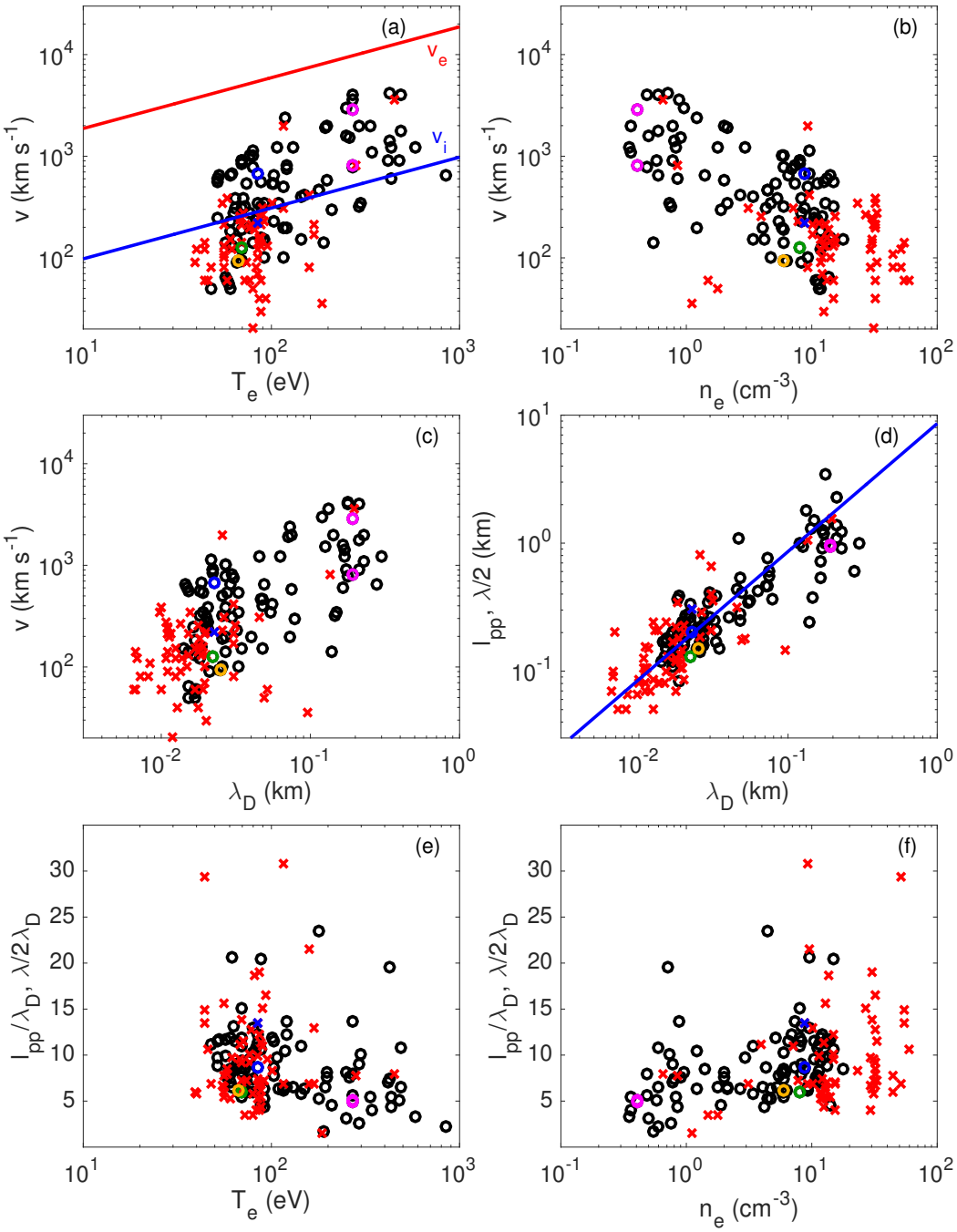

Figure 5. The speeds and length scales of ESWs (black circles) and electrostatic waves (red crosses) compared with the local plasma conditions. (a) v versus T_e (the red line is v_e and the blue line is the nominal v_i assuming $T_i/T_e = 5$). (b) v versus n_e. (c) v versus λ_D. (d) l_{pp} and $\lambda/2$ versus λ_D. The blue line is $l_{pp}, \lambda/2 = 9\,\lambda_D$. (e) l_{pp}/λ_D and $\lambda/2\lambda_D$ versus T_e. (f) l_{pp}/λ_D and $\lambda/2\lambda_D$ versus n_e. The waves in Figures 1, 2, 11, and 13 are represented by the green, blue, orange, and magenta symbols, respectively.

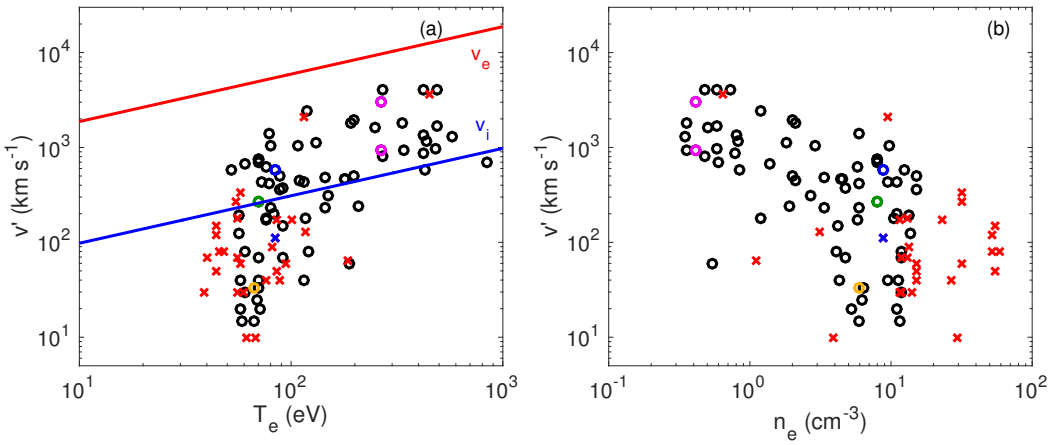

Figure 6. The speeds of ESWs (black circles) and electrostatic waves (red crosses) in the ion frame. (a) v' versus T_e (the red line is v_e and the blue line is the nominal v_i assuming $T_i/T_e = 5$). (b) v' versus n_e. The waves in Figures 1, 2, 11, and 13 are represented by the green, blue, orange, and magenta symbols, respectively.

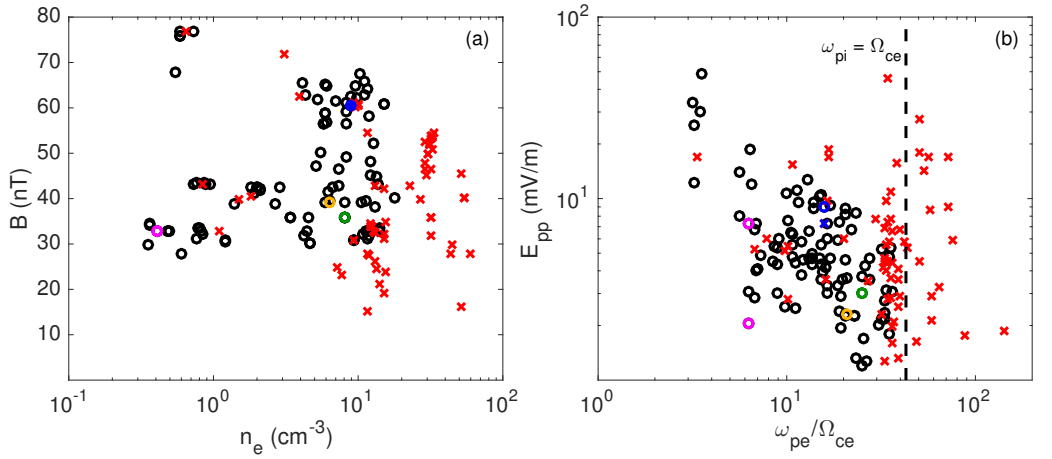

Figure 7. Plots of (a) B versus n and (b) maximum E_{pp} versus ω_{pe}/Ω_{ce} for ESWs (black circles) and electrostatic waves (red crosses). The waves in Figures 1, 2, 11, and 13 are represented by the green, blue, orange, and magenta symbols, respectively.

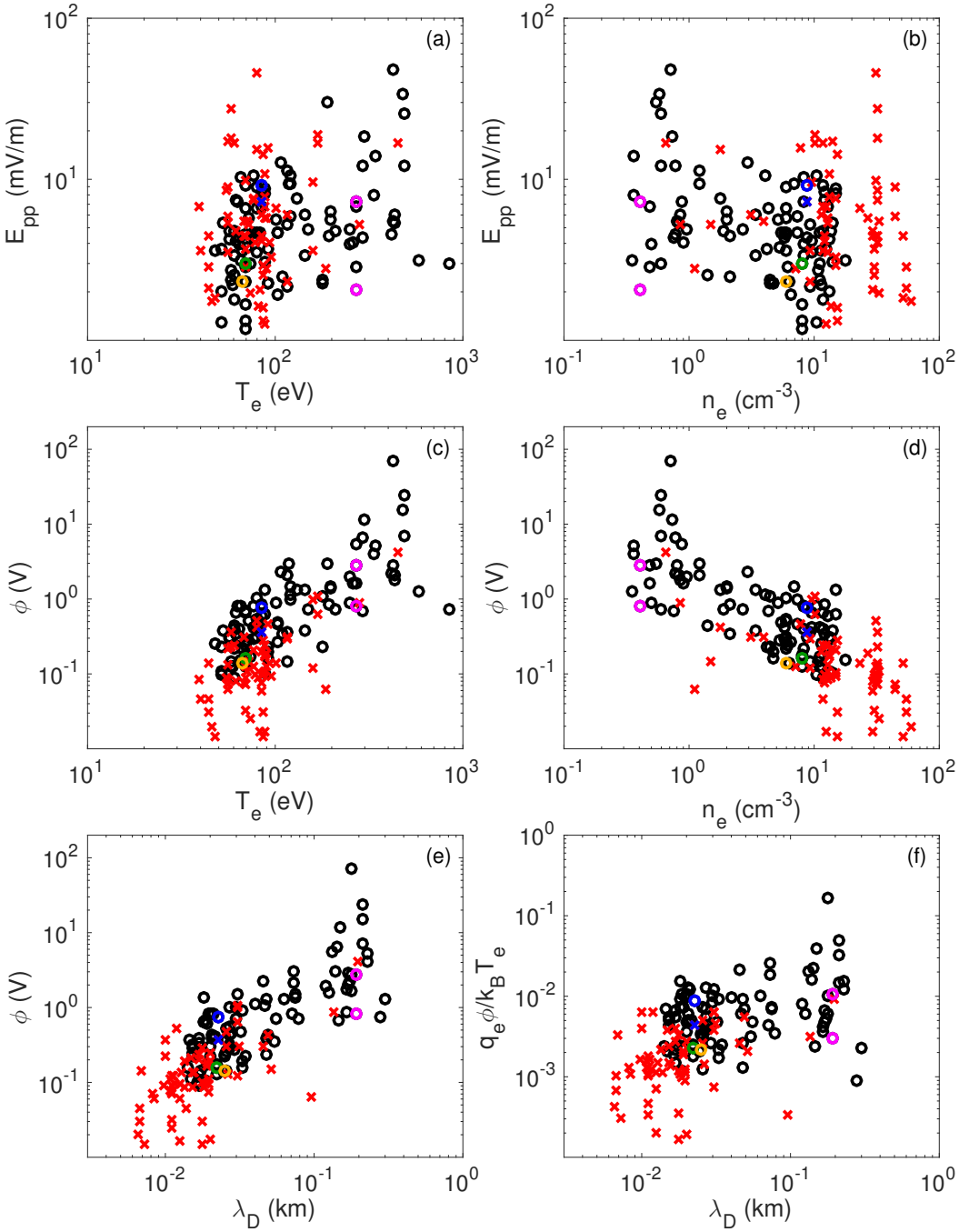

Figure 8. The maximum observed peak-to-peak fields E_{pp} and maximum potentials ϕ of ESWS (black circles) and electrostatic waves (red crosses) versus T_e and n_e for each wave event. (a) and (b) E_{pp} versus T_e and n_e. (c)–(e) Maximum observed potentials $\phi_{\mathrm{ESW,ES}}$ versus T_e, n_e, and λ_D, respectively. (f) Maximum normalized potentials $q_e\phi_{\mathrm{ESW,ES}}/k_BT_e$ versus λ_D. The waves in Figures 1, 2, 11, and 13 are represented by the green, blue, orange, and magenta symbols, respectively.

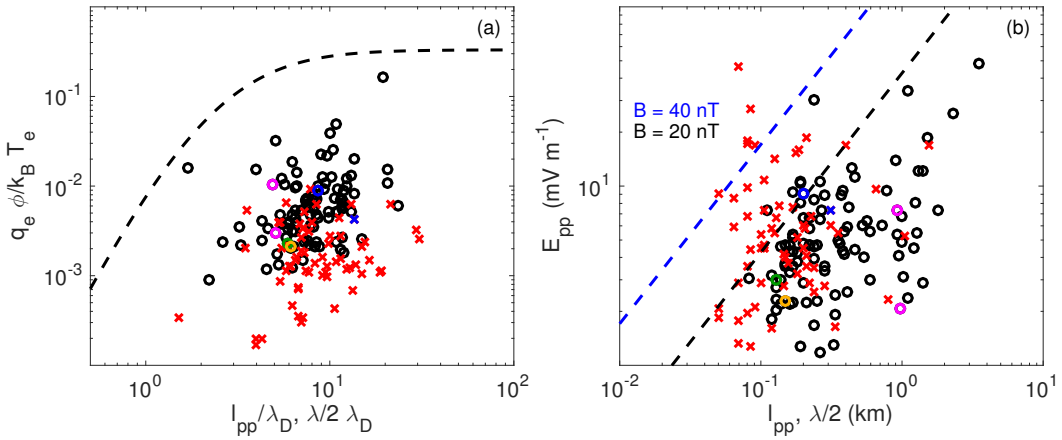

Figure 9. Maximum normalized potentials $q_e\phi/k_BT_e$ and maximum E_{pp} versus length scales of ESWs and electrostatic waves. (a) $q_e\phi/k_BT_e$ versus l_{pp}/λ_D and $\lambda/2\lambda_D$ for ESWs (black circles) and electrostatic waves (red crosses), respectively. The dashed line is the threshold boundary based on equation (11) of *Chen et al.* [2005] for $T_e/T_i = 0.5$ and $l_r/l_\parallel = 4$. The region below the line is consistent with stable electron holes. (b) E_{pp} versus l_{pp} and $\lambda/2$. Overplotted is equation (10) for $B = 20\,\mathrm{nT}$ (black) and $40\,\mathrm{nT}$ (blue). The waves in Figures 1, 2, 11, and 13 are represented by the green, blue, orange, and magenta symbols, respectively.

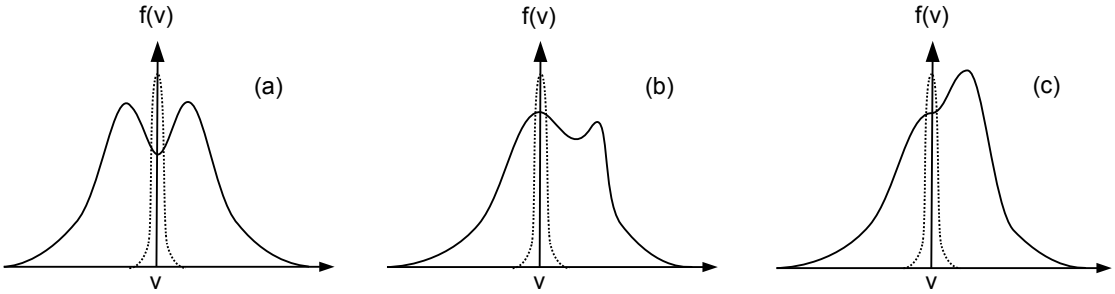

Figure 10. Examples of electron distributions yielding ESWs. (a) Warm bistream instability. (b) Beam-plasma instability. (c) Electron-ion streaming instability. Dotted distributions represent background ions.

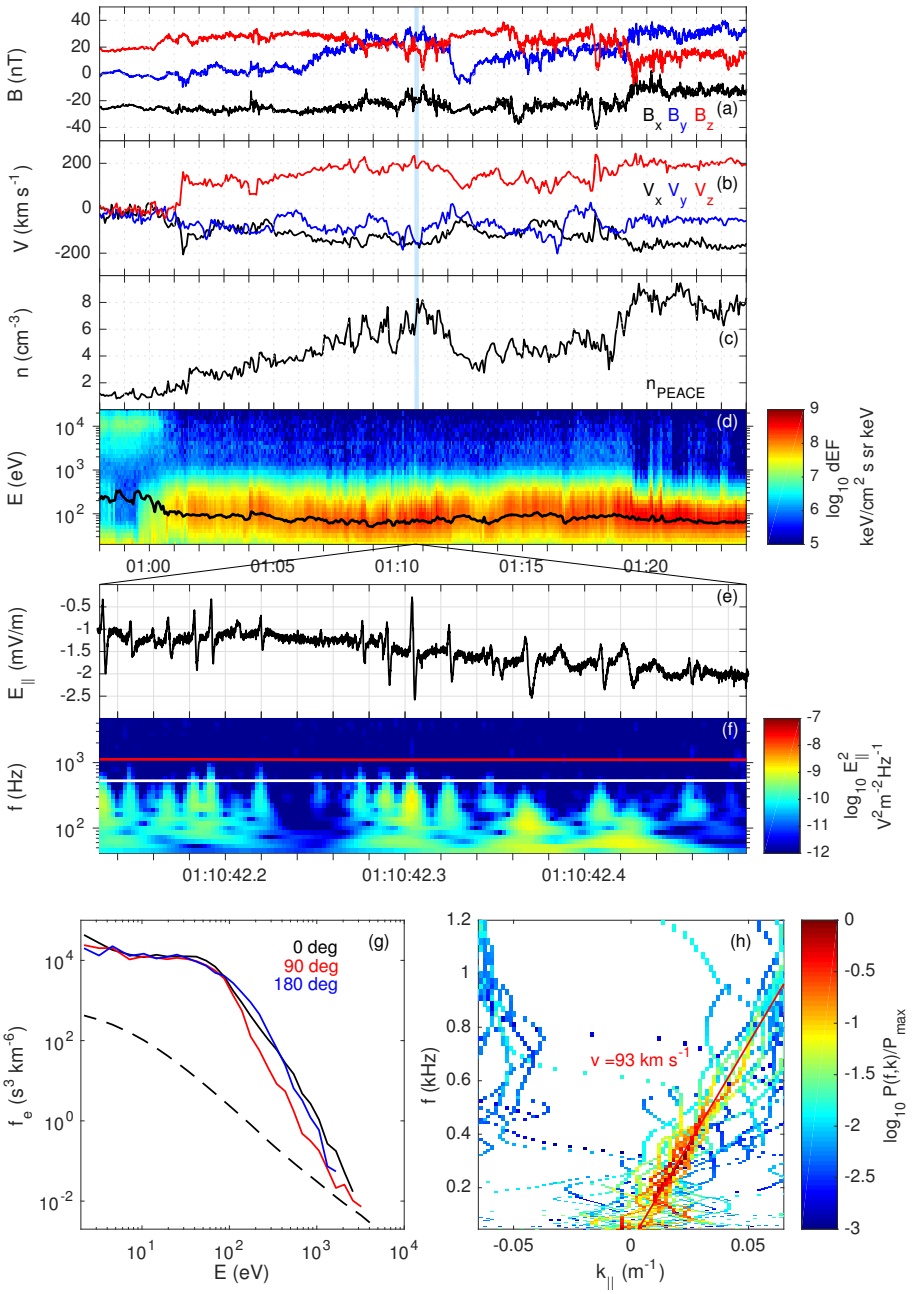

Figure 11. Magnetopause crossing observed by C4 on 22 February 2003. (a) **B** and (b) **V** in GSM coordinates. (c) n_e. (d) Electron differential energy flux (the black line is T_e). The blue shading in (a)–(c) is EFW's internal burst mode interval. (e) $\mathbf{E}_{\|}$ and (f) $\mathbf{E}_{\|}$ spectrogram (the red and white lines are f_{ce} and f_{pi}). (g) $f_e(E)$ versus E averaged over the internal burst mode interval (black, red, and blue curves correspond to $\theta = 0°$, 90°, and 180°, respectively). The dashed line is the instrumental one-count level. (h) Frequency-wave number power spectrum for the ESWs in panel (e).

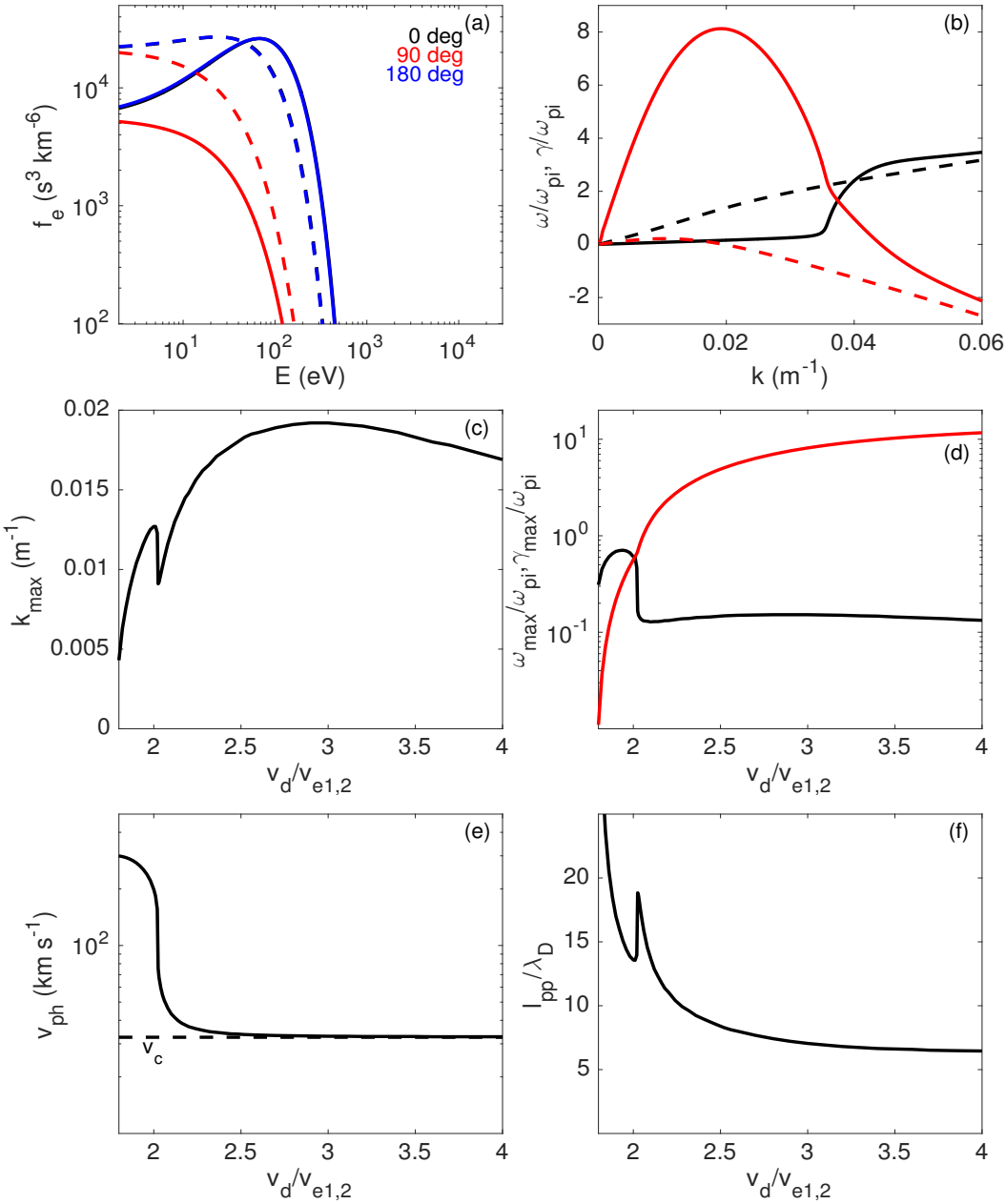

Figure 12. Electron distributions and associated unstable modes for the warm bistream instability. (a) $f_e(E)$ versus E at $\theta = 0°$, 90°, and 180° for electron distributions with $v_d = 3.0v_{e1,2}$ (solid lines) and $1.9v_{e1,2}$ (dashed lines). $f_e(E)$ at $\theta = 0°$ and 180° approximately overlap. (b) Dispersion relations (black) and growth rates (red) for the unstable modes associated with the two electron distributions. The solid and dashed lines correspond to the solutions found for the solid and dashed electron distributions in (a). (c) $k_{\max}$ versus v_d, (d) $\omega_{\max}/\omega_{pi}$ (black) and $\gamma_{\max}/\omega_{pi}$ (red) versus v_d, (e) v_{ph} versus v_d (dashed line is v_c), and (f) l_{pp}/λ_D versus v_d.

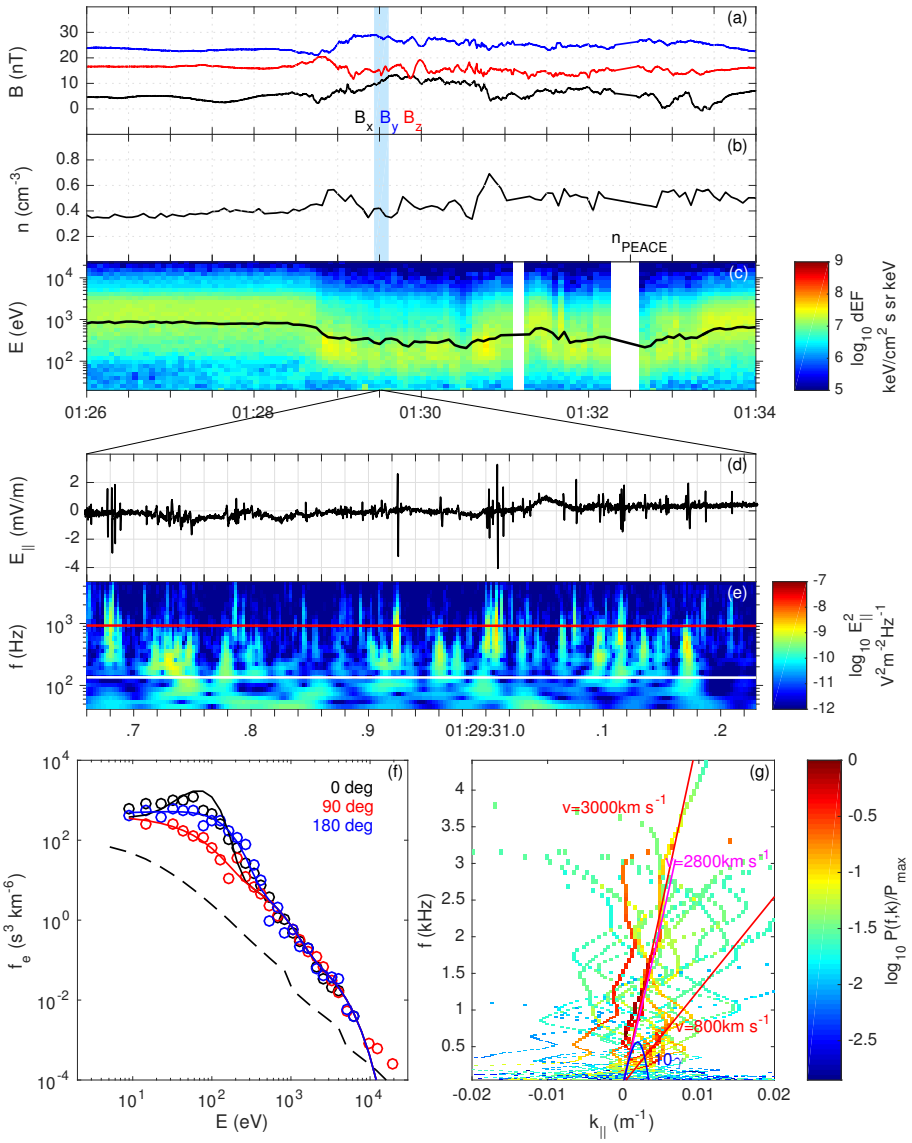

Figure 13. ESW observations by C4 on 28 May 2004 near the magnetopause boundary. (a) **B** (GSM). (b) n_e. (c) Electron differential energy flux (the black line is T_e). The blue shading in (a)–(b) is EFW's internal burst mode interval. (d) $\mathbf{E}_{\|}$ and (e) $\mathbf{E}_{\|}$ spectrogram (the red and white lines are f_{ce} and f_{pi}). (f) Observed $f_e(E)$ versus E (circles) and fit to the data (solid lines) at the time the ESWs were observed (black, red, and blue curves correspond to $\theta = 0°$, $90°$, and $180°$, respectively). The dashed line is the instrumental one-count level. (g) Frequency-wave number power spectrum for the ESWs in panel (d). Red lines are fits to the data, and the magenta and blue lines are the predicted dispersion relation and growth rate for the fitted $f_e(E)$.